





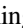




















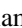












TESS Eclipsing Binary Stars. I. Short-cadence Observations of 4584 Eclipsing Binaries in Sectors 1–26

Andrej Prša¹ , Angela Kochoska¹ , Kyle E. Conroy¹ , Nora Eisner² , Daniel R. Hey³ , Luc IJspeert⁴, Ethan Kruse⁵ , Scott W. Fleming⁶ , Cole Johnston^{4,7}, Martti H. Kristiansen^{8,9} , Daryll LaCourse¹⁰ , Danielle Mortensen¹, Joshua Pepper¹¹ , Keivan G. Stassun¹² , Guillermo Torres¹³ , Michael Abdul-Masih¹⁴ , Joheen Chakraborty¹⁵, Robert Gagliano¹⁶, Zhao Guo¹⁷ , Kelly Hambleton¹ , Kyeongsoo Hong¹⁸ , Thomas Jacobs¹⁹ , David Jones^{20,21} , Veselin Kostov^{5,22} , Jae Woo Lee²³ , Mark Omohundro²⁴, Jerome A. Orosz²⁵ , Emma J. Page¹¹, Brian P. Powell⁵ , Saul Rappaport²⁶ , Phill Reed²⁷ , Jeremy Schnittman²⁸, Hans Martin Schwengeler²⁹ , Avi Shporer³⁰ , Ivan A. Terentev³¹, Andrew Vanderburg³² , William F. Welsh²⁵ , Douglas A. Caldwell^{33,34} , John P. Doty³⁵ , Jon M. Jenkins³⁴ , David W. Latham³⁶ , George R. Ricker²⁶ , Sara Seager^{26,37,38}, Joshua E. Schlieder³⁹ , Bernie Shiao⁴⁰, Roland Vanderspek²⁶ , and Joshua N. Winn⁴¹ 

¹ Villanova University, Dept. of Astrophysics and Planetary Sciences, 800 East Lancaster Avenue, Villanova, PA 19085, USA; aprs@villanova.edu

² University of Oxford, Department of Physics, Keble Road, Oxford OX1 3RH, UK

³ School of Physics, Sydney Institute for Astronomy (SIFA), The University of Sydney, NSW 2006, Australia

⁴ KU Leuven, Institute of Astronomy, Celestijnenlaan 200D, B-3001, Leuven, Belgium

⁵ NASA Goddard Space Flight Center, 8800 Greenbelt Road, Greenbelt, MD 20771, USA

⁶ Space Telescope Science Institute, 3700 San Martin Drive, Baltimore, MD 21218, USA

⁷ Radboud University Nijmegen, Department of Astrophysics, IMAPP, P.O. Box 9010, 6500 GL Nijmegen, The Netherlands

⁸ Brorfelde Observatory, Observator Gyldenkernes Vej 7, DK-4340 Tølløse, Denmark

⁹ DTU Space, National Space Institute, Technical University of Denmark, Elektrovej 327, DK-2800 Lyngby, Denmark

¹⁰ Amateur Astronomer, 7507 52nd Place NE, Marysville, WA 98270, USA

¹¹ Lehigh University, Department of Physics, 13 Memorial Drive East, Bethlehem, PA 18015, USA

¹² Vanderbilt University, Department of Physics & Astronomy, 6301 Stevenson Center Lane, Nashville, TN 37235, USA

¹³ Harvard Smithsonian Center for Astrophysics, 60 Garden Street, Cambridge, MA 02138, USA

¹⁴ European Southern Observatory, Alonso de Cordova 3107, Vitacura, Casilla 19001, Santiago de Chile, Chile

¹⁵ Columbia University, Department of Astronomy, 550 West 120th Street, New York, NY 10027, USA

¹⁶ Amateur Astronomer, Glendale, AZ, USA

¹⁷ University of Cambridge, Department of Applied Mathematics and Theoretical Physics, Centre for Mathematical Sciences, Wilberforce Road, Cambridge CB3 0WA, UK

¹⁸ Institute for Astrophysics, Chungbuk National University, Chungdae-ro 1, Seowon-Gu, Cheongju 28644, Republic of Korea

¹⁹ Amateur Astronomer, 12812 SE 69th Place, Bellevue, WA 98006, USA

²⁰ Instituto de Astrofísica de Canarias, E-38205 La Laguna, Tenerife, Spain

²¹ Departamento de Astrofísica, Universidad de La Laguna, E-38206 La Laguna, Tenerife, Spain

²² SETI Institute, Mountain View, CA, USA

²³ Korea Astronomy and Space Science Institute, Optical Division, 776 Daedeok-daero, Yuseong-gu, Daejeon 34055, Republic of Korea

²⁴ Citizen scientist, c/o Zooniverse, Department of Physics, University of Oxford, Denys Wilkinson Building, Keble Road, Oxford, OX1 3RH, UK

²⁵ San Diego State University, Department of Astronomy, 5500 Campanile Drive, San Diego, CA 92182-1221, USA

²⁶ Department of Physics and Kavli Institute for Astrophysics and Space Research, Massachusetts Institute of Technology, Cambridge, MA 02139, USA

²⁷ Department of Physical Sciences, Kutztown University, Kutztown, PA 19530, USA

²⁸ NASA Goddard Space Flight Center, Astrophysics Science Division, 8800 Greenbelt Road, Greenbelt, MD 20771, USA

²⁹ Citizen Scientist, Zehntenfreistrasse 11, CH-4103 Bottmingen, Switzerland

³⁰ Massachusetts Institute of Technology, Department of Physics and Kavli Institute for Astrophysics and Space Research, Cambridge, MA 02139, USA

³¹ Citizen Scientist, Moskovskaya 8, 185031 Petrozavodsk, Russia

³² Department of Physics and Kavli Institute for Astrophysics and Space Research, Massachusetts Institute of Technology, 77 Massachusetts Avenue, Cambridge, MA 02139, USA

³³ SETI Institute, 189 Bernardo Avenue, Suite 200, Mountain View, CA 94043, USA

³⁴ NASA Ames Research Center, Moffett Field, CA 94035, USA

³⁵ Noqsi Aerospace Ltd., 15 Blanchard Avenue, Billerica, MA 01821, USA

³⁶ Harvard-Smithsonian Center for Astrophysics, 60 Garden Street, Cambridge, MA 02138, USA

³⁷ Department of Earth, Atmospheric and Planetary Sciences, Massachusetts Institute of Technology, Cambridge, MA 02139, USA

³⁸ Department of Aeronautics and Astronautics, MIT, 77 Massachusetts Avenue, Cambridge, MA 02139, USA

³⁹ NASA Goddard Space Flight Center, 8800 Greenbelt Road, Greenbelt, MD 20771, USA

⁴⁰ Space Telescope Science Institute, 3700 San Martin Drive, Baltimore, MD, 21218, USA

⁴¹ Department of Astrophysical Sciences, Princeton University, 4 Ivy Lane, Princeton, NJ 08544, USA

Received 2021 October 4; revised 2021 October 19; accepted 2021 October 20; published 2022 January 12

Abstract

In this paper we present a catalog of 4584 eclipsing binaries observed during the first two years (26 sectors) of the TESS survey. We discuss selection criteria for eclipsing binary candidates, detection of hitherto unknown eclipsing systems, determination of the ephemerides, the validation and triage process, and the derivation of heuristic estimates for the ephemerides. Instead of keeping to the widely used discrete classes, we propose a binary star



Original content from this work may be used under the terms of the [Creative Commons Attribution 4.0 licence](https://creativecommons.org/licenses/by/4.0/). Any further distribution of this work must maintain attribution to the author(s) and the title of the work, journal citation and DOI.

morphology classification based on a dimensionality reduction algorithm. Finally, we present statistical properties of the sample, we qualitatively estimate completeness, and we discuss the results. The work presented here is organized and performed within the TESS Eclipsing Binary Working Group, an open group of professional and citizen scientists; we conclude by describing ongoing work and future goals for the group. The catalog is available from <http://tessEBs.villanova.edu> and from MAST.

Unified Astronomy Thesaurus concepts: [Eclipsing binary stars \(444\)](#); [Catalogs \(205\)](#); [Sky surveys \(1464\)](#); [Photometry \(1234\)](#); [Light curves \(918\)](#); [Fundamental parameters of stars \(555\)](#)

1. Introduction

The Transiting Exoplanet Survey Satellite (TESS; Ricker et al. 2015) was launched in 2018 April; during its 2 yr prime mission, it monitored $\sim 200,000$ bright stars for exoplanets across the sky with a 2 minute short cadence. In addition, TESS acquired full-frame images (FFIs) every 30 minutes. TESS is currently in its extended mission, where targets are observed with a 2 minute and a 20 s cadence, and FFIs are acquired every 10 minutes. The primary TESS mission has been to discover and characterize exoplanets, but TESS data enable a much broader swath of science—all fields that benefit from precise time series of bright stars, in fact—including eclipsing binary systems.

Eclipsing binaries (EBs) serve as one of the pillars of stellar astrophysics. The well-understood laws of motion that govern binarity and the alignment with the line of sight make their analysis a tractable geometrical problem (Prša 2018), yielding accurate masses, radii, temperatures, and luminosities of EB components (Torres et al. 2010). Because of that, EBs are used to calibrate stellar models across the Hertzsprung–Russell diagram (Serenelli et al. 2021), rendering them important to essentially every field in astronomy.

Binary stars are ubiquitous: more than half the stars with masses of $1 M_{\odot}$ or higher are found in binary or multiple systems (Raghavan et al. 2010; Sana’ et al. 2012; Moe & Di Stefano 2017). Binaries are thus a natural product of star formation and make up a large fraction of the visible universe. Understanding binaries means understanding stellar formation and evolution (Stacy et al. 2010), internal stellar structure by way of tidal interactions, and/or tidally induced pulsations (Thompson et al. 2012), accretion physics in semi-detached binaries (Bisikalo 2010), and much more. At the same time, there are many open questions that remain; for example, what mechanism (or combination of mechanisms) drives multiplicity rates (Duchêne & Kraus 2013), what determines the distribution of mass ratios (Wells & Prša 2021), how does (close) binarity affect stellar evolution of stars (blue stragglers, yellow giants, magnetic interaction; Mathieu & Geller 2009), how does orbital tightening work given that the Kozai–Lidov cycles might not fully explain it (Hwang & Zakamska 2020), and how do exoplanets that orbit binary stars form and evolve (Paardekooper et al. 2012)? It is *eclipsing* binaries that hold the answer to these and similar questions. Astronomers have studied EBs for over two centuries, ever since John Goodricke suggested in 1782 that eclipses are responsible for Algol’s brightness variation. So why are the answers so elusive?

The principal reason for the remaining open questions is that traditional observational techniques (ground-based photometry, follow-up spectroscopy, long baseline interferometry) are best suited to single objects and are time-consuming. Thus, it is difficult to draw inferences on the entire population of binaries. The first mission that made a significant breakthrough in the EB science was Kepler (Kirk et al. 2016a), but the downside of

Kepler is that its targets are faint (i.e., difficult to follow up), limited to a single ~ 100 deg² field, and telemetry and onboard storage did not allow FFIs to be sent back to Earth. Those obstacles are largely overcome by TESS: TESS observes on the bright end, targets are sourced across the sky, and we have 10 minute FFIs. These benefits come at the expense of large (21’’) pixels adversely affecting crowded fields, but TESS still serves as a proverbial gold mine for EBs away from the Galactic plane.

EBs play a less celebrated role in exoplanetary science, where $\sim 40\%$ of false positives at low Galactic latitudes are attributed to their diluted light curves (Morton & Johnson 2011). About 25% of TESS objects of interest (TOIs) that were examined by ground-based photometric follow-up turned out to be background binaries. Thus, having a good census of EBs feeds back to identifying false positives before pointing costly follow-up telescopes in their direction.

In this paper, the first in the TESS EB series, we present a sample of 4584 EBs observed by TESS in the first 26 sectors of observation. In Section 2 we describe light-curve detection and identification, in Section 3 we explain how ephemerides for each system are determined and refined, in Section 4 we present an automated data validation pipeline called ICED LATTE, in Section 5 we focus on statistical properties of the EB sample and qualitatively assess completeness, in Section 6 we describe the contents of the catalog, and finally, in Section 7 we discuss some of the most interesting results and provide a list of ongoing projects and future goals for the working group.

2. Detection of TESS EBs

Extracting a sample of EBs from the observations of $\sim 200,000$ 2 minute cadence light curves involved multiple complementing efforts. We describe these efforts here.

Proposed targets: As part of the TESS Guest Investigator program, we proposed 3889 targets in Cycle 1 and 3067 targets in Cycle 2. The targets were selected from all public binary star catalogs served on VizieR (Ochsenbein et al. 2000), the General Catalog of Variable Stars (GCVS; Samus et al. 2017), and the Spectroscopic Binary Catalog (SB9; Pourbaix et al. 2004). The proposed targets were prioritized by a multitude of factors: (1) spatial position in the sky, i.e., the number of visits, (2) T magnitude, as it appears in the TESS Input Catalog (TIC; Stassun et al. 2018), (3) membership in the Detached Eclipsing Binary Catalog (DEBCAT; Southworth 2015), (4) classification certainty, and (5) scientific importance. Each criterion was assigned a numerical value (positive or negative) and their sum determined a priority value in the target list. Thus, bright DEBCAT members in the continuous viewing zone were the highest priority targets. Targets on the faint end observed in a single sector and without certain classification were the lowest priority targets. Of the proposed targets, 745 were selected for observations in Cycle 1 and 999 were selected for observations in Cycle 2.

A total of 6699 EB candidates were identified via the Planet Hunters TESS (PHT) citizen science project (Eisner et al. 2021), which is hosted by the Zooniverse platform (Lintott et al. 2008, 2011). The project engages over 30,000 registered citizen scientists in the search for transiting exoplanets in the 2 minute cadence light curve obtained by TESS. The identification of eclipsing binaries and multi-stellar systems is a natural by-product of this large-scale visual vetting effort. In brief, each 2 minute cadence TESS light curve is visually inspected by 15 citizen scientists who identify the times of any transit-like signals before moving on to the next light curve. Once all of the data from a given TESS sector have been classified, the classifications from the individual volunteers are combined using an unsupervised machine-learning algorithm. This allows us to identify times of potential transit-like events in each light curve and rank all of the candidates from most to least likely to contain a transit signal (for details, see Eisner et al. 2021). The 500–700 highest ranked candidates per sector are visually inspected by the PHT science team and grouped into “planet candidates,” “EB candidates,” and “other.” In total, we identified 2720 EB candidates using this methodology.

In addition to this classification pipeline, each target has an independent discussion forum where the citizen scientists can discuss the data and flag the signals to the science team using searchable hashtags. By the end of the primary mission, the tags “EB,” “eclipsing binary,” or similar versions thereof had appeared over 46,200 times on the discussion forums, corresponding to 5759 individual TESS targets. All of these targets were considered as potential EB candidates and were kept for further vetting. A total of 1780 candidates were discovered via both of these methods, bringing the total number of EB candidates identified via PHT to 6699.

A second manual search for TESS EBs was carried out by another team of seven citizen scientists, the Visual Survey Group (VSG), independently of the PHT effort. Up until Sector 21, the VSG collectively scrutinized the Candidate Target List light curves (CTL; Stassun et al. 2018) which were binned at six points per hour. Data from subsequent sectors were binned at two points per hour. All data were prepared and surveyed with the LcTools software (Schmitt & Vanderburg 2021) from FITS files stored at the Mikulski Archive for Space Telescopes (MAST).

The Weird Detector pipeline: Wheeler & Kipping (2019) introduced the Weird Detector, a phase-dispersion-based periodic signal-detection algorithm with minimal requirements for signal morphology. The merit function (ζ) of a given trial period (P_{trial}) is calculated using (I) local decrease in χ^2 of the binned, phase-folded light curve and (II) the kurtosis characterizing the tailedness of the binned flux distribution to ensure a mostly flat baseline with one (or a few) excursion(s) representing a dimming event. Chakraborty et al. (2020) applied the algorithm to 248,000 2 minute light curves from the first 13 sectors of TESS data; given the highly general nature of the algorithm’s candidate signal-finding goal—no particular target shape is optimized for in the pipeline’s signal-finding process—the relatively higher signal-to-noise ratio (S/N) of eclipsing binaries compared with many other periodic sources makes them a large fraction (313/377) of the candidate signals. All candidates from this pool were manually vetted, ultimately yielding no novel detections, but with an overlap of 265 true-positive signals.

SPOC pipeline: All TESS 2 minute pixel stamps are processed by the Science Processing Operations Center (SPOC) pipeline (Jenkins et al. 2016). The pipeline runs optimal photometric extraction, followed by two types of light curves: simple aperture photometry (SAP) and pre-search data-conditioning (PDC) light curves. The SAP light curves are background-corrected, but have no additional detrending, while constructing the PDC light curves includes detrending for common-mode instrumental systematics using co-trending basis vectors empirically calculated from other sources on the corresponding detector (Smith et al. 2012; Stumpe et al. 2014). The PDC light curves are also corrected for flux contamination from nearby stars. Here we chose to use the SAP light curves to avoid cases where the detrending affects the astrophysical signal (Twicken et al. 2010; Stumpe et al. 2012; Morris et al. 2020).

The SPOC pipeline also searches the PDC light curves for transiting planet signatures using an adaptive, wavelet-based matched filter (Jenkins 2002; Jenkins et al. 2010), and the resulting TCEs are fitted with an initial limb-darkened transit model (Li et al. 2019) and subjected to a suite of diagnostic tests to help determine whether the transit signature is due to a planet, an eclipsing binary, stellar variability, or an instrumental effect.

3. The Determination of EB Ephemerides

3.1. The QATS Code

The Quasiperiodic Automated Transit Search (QATS) is a pipeline originally developed to find planets with transit timing variations in the Kepler data (Carter & Agol 2013). It was subsequently updated and revised to be a more general planet and eclipsing binary search tool, as first applied to K2 by Kruse et al. (2019). The implementation used here is identical to that of Kruse et al. (2019), so we refer the reader there for full details. In brief, QATS models a transit at every cadence in a light curve and compares that model’s χ^2 fit to a pure polynomial continuum. It then runs a period-folding search over that sequence of $\Delta\chi^2$ to identify periodic signals where the transit fit is better than the continuum. Once it has identified a candidate periodic signal, it runs a more thorough transit fit to accurately measure the transit or eclipse parameters.

3.2. The ECLIPSR Code

ECLIPSR (Eclipse Candidates in Light curves and Inference of Period at a Speedy Rate; Ijspeert et al. 2021) is an algorithm that operates in two main stages: finding eclipses in the light curve and subsequently determining the periodicity in those eclipses. Finding (individual) eclipses in the light curve is achieved by looking for peaks in its time derivatives. This enables the successful identification of eclipses in light curves that show strong additional (intrinsic) variability compared to the eclipse signal. This process is fully automated and produces a score at the end for each light curve that can be used to separate light curves that show eclipses from those that do not contain an eclipse signal. Here, we start off from a list of pre-determined EB candidates and use the ECLIPSR algorithm mainly for its ability to determine ephemerides.

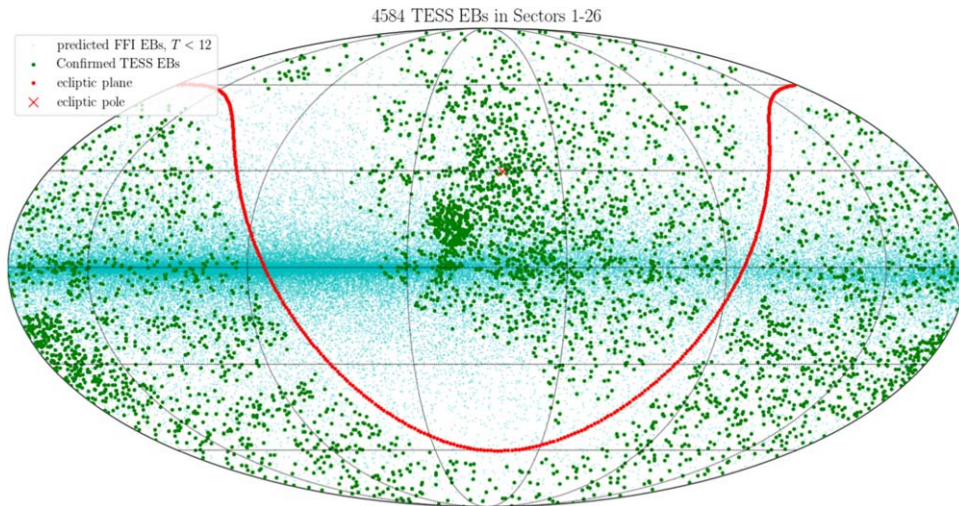


Figure 1. Map of TESS EBs observed in sectors 1–26 in the Galactic reference frame. Depicted in green are all vetted and validated EBs observed with the 2 minute cadence. Depicted in cyan are the simulated EBs brighter than $T = 12$ (Wells & Prša 2021). The dearth of systems in the region north of the ecliptic plane is due to the change in boresight in sectors 14–16 and 24–26, where the satellite was pointed at $+85^\circ$ instead of the nominal $+54^\circ$ to mitigate excessive contamination by stray Earth light and moonlight in cameras 1 and 2.

3.3. The BLS Run

The final algorithm employed a traditional and well-tested approach to searching for transit-like signals: the box least squares (BLS) periodogram (Kovács et al. 2002). In the BLS periodogram, a sliding box-like signal is passed over the light curve for a range of orbital periods and the likelihood of the model is recorded at each orbital period. The resulting periodogram is expected to peak at integer multiples of any box-like periodic signals in the light curve, thus it is well-suited to the detection of eclipses. We used the BLS implementation in Astropy (Astropy Collaboration et al. 2013) with the LIGHTKURVE package (Barentsen et al. 2019) to normalize and prepare the light curves. No further pre-processing was applied to the light curve beyond a simple normalization of flux. Although straightforward to implement and run, the BLS algorithm relies on strictly periodic signals and thus cannot identify single eclipse events. The orbital periods searched by BLS ranged from 0.1 days to half the timespan of the light curve, with an oversampling factor of 20.

3.4. Triage

All candidate targets were vetted manually by at least one of the authors through a custom web application. For each TIC entry, phased plots were shown at the period, as well as half period and double period, for each of the automated ephemeris algorithms discussed above.

The triage user would then choose which period (if any) correctly represented the signal and classify whether the signal was that of an eclipsing binary or some other variable source. Subcategories were available to flag eclipsing binaries where the period was ambiguous (whether there are two nearly identical primary and secondary eclipses or no visible secondary eclipse) and whether there was an insufficient number of eclipses in the data to accurately determine the orbital period.

Ephemerides for a single TIC target with periods (or period multiples) within 1% were automatically flagged as representing the same underlying signal. All other multiple ephemerides classified as eclipsing binary signals were then treated

independently as either blended EBs or true hierarchical systems.

A total of 27,496 candidate ephemerides (from 10,477 unique TICs) and their half- and double-period counterparts were triaged. Of those, 4592 ephemerides (from 4584 unique TICs) were manually classified as likely being caused by an eclipsing binary signal (see Figure 1) and were passed on to the ephemeris refinement algorithm described below. Additionally, 520 input ephemerides (from 457 unique TICs) were classified as likely eclipsing binaries but with an insufficient number of eclipses to determine an orbital period. We flagged 1872 input ephemerides (from 1725 unique TICs) as requiring further follow-up to determine whether they were eclipsing binaries or pulsating stars (due to sinusoidal signals), 9434 input ephemerides (from 6029 unique TICs) were classified as having no eclipsing binary signal, and 11,078 input ephemerides were marked as duplicates of another ephemeris entry for the same TIC. Figure 2 depicts several exemplary EB light curves from the TESS catalog.

3.5. Refinement and Heuristic Error Estimates

To further refine the ephemerides determined from triage, we fit analytical models to the phase-folded light curves and sample the posteriors of the period used for phase-folding and the model parameters. The two analytical models used are two-Gaussian (Mowlavi et al. 2017) and polyfit (Prša et al. 2008).

The two-Gaussian models fit a phased light curve by using one or two Gaussian functions and/or a cosine function with its maximum coinciding with one of the eclipses. The Gaussians are supposed to fit eclipses and the cosine function is supposed to fit symmetric ellipsoidal variability. The light curve is fit by all combinations of functions and it finds the solution that minimizes the degrees of freedom while retaining a satisfactory fit. The model with the highest Bayesian information criterion (BIC) is chosen as the best fit and used in the subsequent analysis. The left panels in Figure 3 depict an example of a two-Gaussian fit.

The polyfit analytical model relies on fitting a piecewise-connected chain of polynomials to the phased light curve. The constraints imposed on the chain are that it should be connected

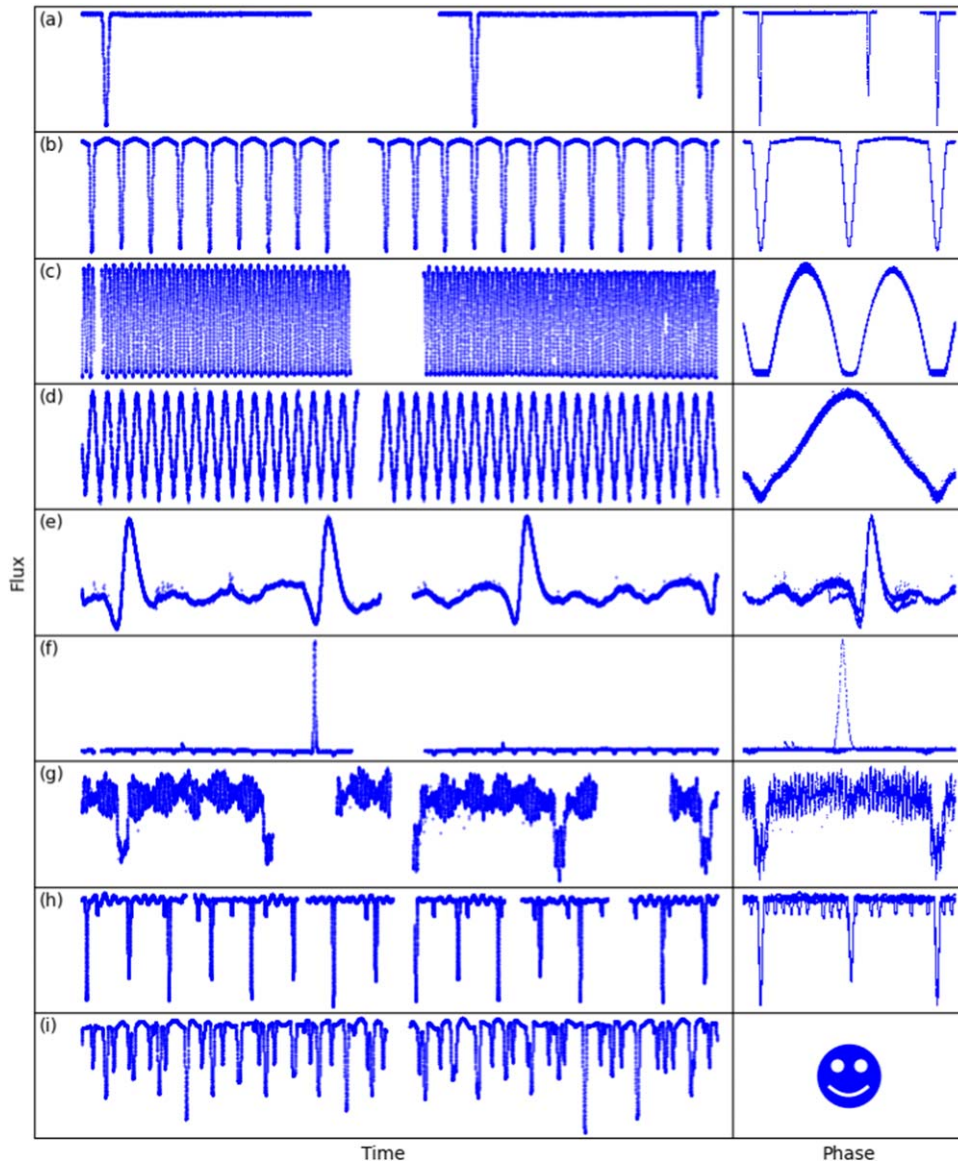


Figure 2. A showcase of interesting objects observed by TESS. The panels on the left display time series and the panels on the right depict phase plots. The objects are, top to bottom: (a) wide eclipsing binary TIC 24935204, (b) benchmark-grade eclipsing binary TIC 33419790, (c) totally eclipsing contact binary TIC 5674169, (d) high-reflection subdwarf binary TIC 31690845, (e) eccentric ellipsoidal binary TIC 11046410, (f) flaring M-dwarf pair TIC 436869712, (g) eclipsing binary with a pulsating component TIC 10891640, (h) multiple signal eclipsing binary TIC 375422201, and (i) quadruple star system TIC 424508303.

and smoothly wrapped in phase space. There is no requirement that the chain be differentiable in the knots, which allows it to easily fit the discrete breaks caused by eclipses. As such, the knots are typically positioned at the ingress and egress of the eclipses. We use four quadratic polynomials connected at four knots. The right panels in Figure 3 depict an example of a polyfit.

The light-curve geometries induced by the eclipses, ellipsoidal variability, spots, and other potentially present signals are in reality more complex than those that can be modeled with these analytical functions. However, they are sufficient for this preliminary analysis which focuses on period refinement and simple geometrical parameter estimates.

To estimate the initial distributions for the model parameters, we first fit the model to the phase-folded data. For the two-Gaussian model, the best-fitting combination of eclipses and a cosine term are chosen and their corresponding parameters passed on to a Markov Chain Monte Carlo (MCMC) search with walkers initialized in a tight ball around the fitted

parameter values. If there are no eclipses or ellipsoidal variability detected by two Gaussians (which results in a constant function fit), the light curve is not passed on to MCMC and flagged as “failed two-Gaussian.” Similarly, we fit an initial polyfit to the phase-folded light curve, and if successful, we initialize a sample around the fitted knot positions and polynomial coefficients. A failed polyfit is rare, but if the algorithm raises any errors that do not result in a fit, we flag that system as a “failed polyfit.”

We run MCMC with EMCEE (Foreman-Mackey et al. 2019) on each candidate EB light curve with 96 walkers for 2000 iterations. The burn-in typically takes under 100 iterations, but we discard the first 1000 iterations for the mean and standard deviation computation of the parameter posteriors. We also check for potential multiple “branches” of walkers at different log probabilities and only use the one with the lowest log probability of the posteriors. Out of the 4584 EB candidates, 98.08% were successfully fitted with a two-Gaussian model and

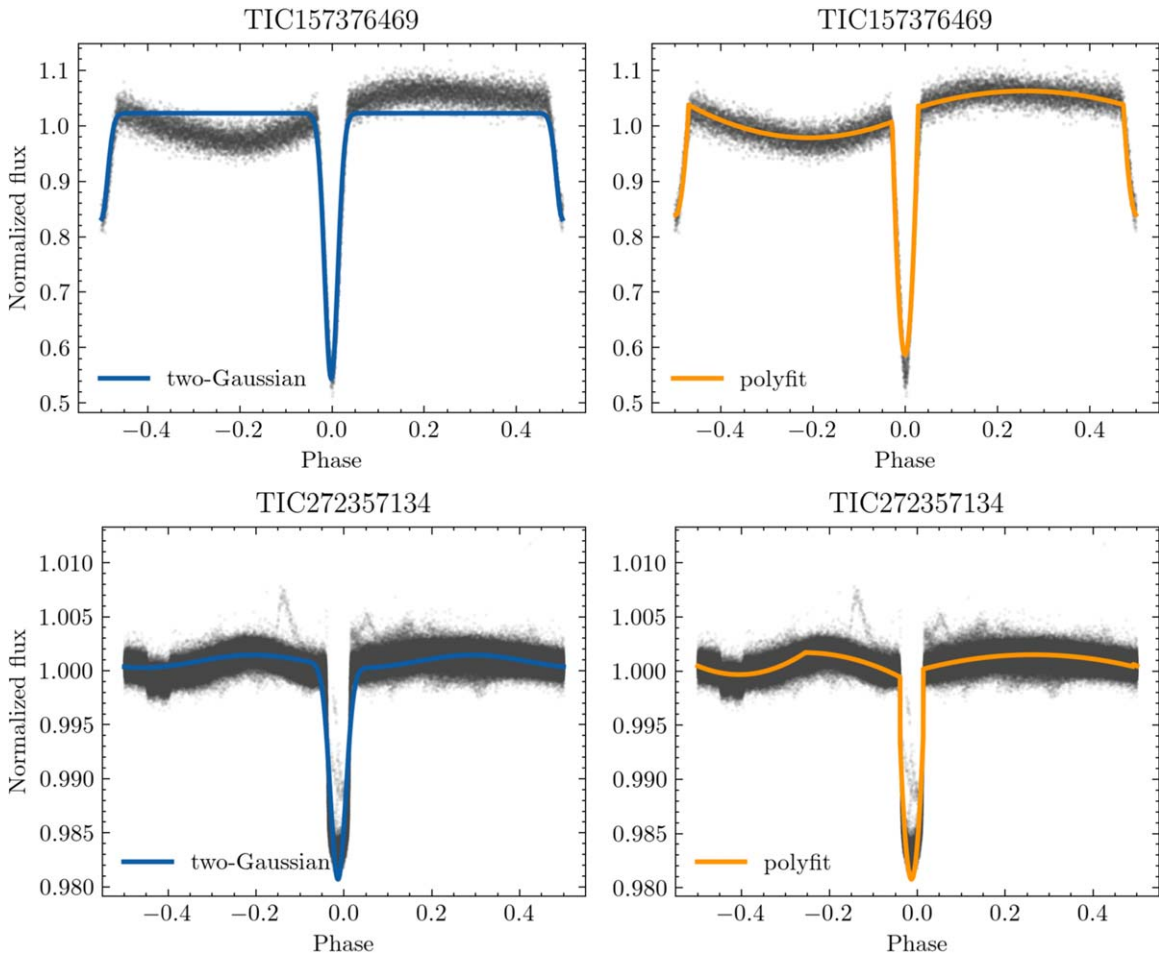


Figure 3. Demonstration of a successful (top panels) and unsuccessful (bottom panels) fit with the two models. The top panels show a system with asymmetric variability outside of eclipse, which cannot be modeled by the two-Gaussian model. However, this does not prevent the model from fitting the eclipses correctly. Polyfit, due to its higher degree of freedom, manages to capture both the eclipses and variability outside of eclipse. The bottom panels show the deficiencies of the two models that cause it to not correctly fit the shallow secondary eclipse: the two-Gaussian model considers it part of the asymmetric variability outside of eclipse that it is unable to model, while polyfit fits the variability as an eclipse instead.

99.85% with polyfit. Out of the fitted two Gaussians, 99.24% within 1% of the triage period, and 98.89% of the fitted polyfits are within 1% of the triage period. Additionally, 98.93% of fitted two Gaussians are within 1% of the polyfit periods.

As depicted in Figure 3, two-Gaussian and polyfit have their deficiencies which hinder their application to all systems. Fortunately, they tend to complement each other (unlike two-Gaussian, polyfit can fit a wide range of out-of-eclipse signals, including highly asymmetric ones; while two-Gaussians will tend to fit eclipses even in noisy data, where polyfit underperforms). We also run additional checks to ensure that a fitted Gaussian or polyfit truly fits an eclipse and not some other feature of the light curve:

1. overlapping eclipses check—ensures that a single eclipse is not fitted by two Gaussians or two polynomials;
2. noise check—ensures that a Gaussian is not fitted to the data noise;
3. ELV check—ensures that a Gaussian is not fitted to ellipsoidal variations (ELVs) or another out-of-eclipse variability;
4. polyfit only: check that the eclipse coincides with a polynomial minimum and not a knot position. If a knot exists with a lower flux value than the polynomial minimum, the eclipse is discarded.

Where any one of these checks fails, the eclipse parameters are not reported, even if a two-Gaussian or polyfit model solution exists.

To fully utilize the information returned from both models and their period and parameter distribution, we compute combined ephemerides, which are ultimately reported in the catalog. The combined ephemerides are computed by sampling both the two-Gaussian and polyfit distributions, under the constraint that the number of samples drawn from each distribution is inversely proportional to the reduced χ^2 value (chi_r^2) of the mean fit (Figure 4). The mean and standard deviation of the new combined distribution are then chosen as the final ephemerides. We perform an additional check to ensure that the models whose distributions we sample are reasonable. If a model reports uncertainty of the time of superior conjunction larger than half the fitted period, the time of superior conjunction for that model is discarded. This happens more often in the case of polyfit, as the eclipse model has more degrees of freedom.

3.6. Morphology Classification

For morphological classification of the light curves, we rely on the morphology parameter as defined in Matijevič et al. (2012). The morphology parameter is defined as a continuous

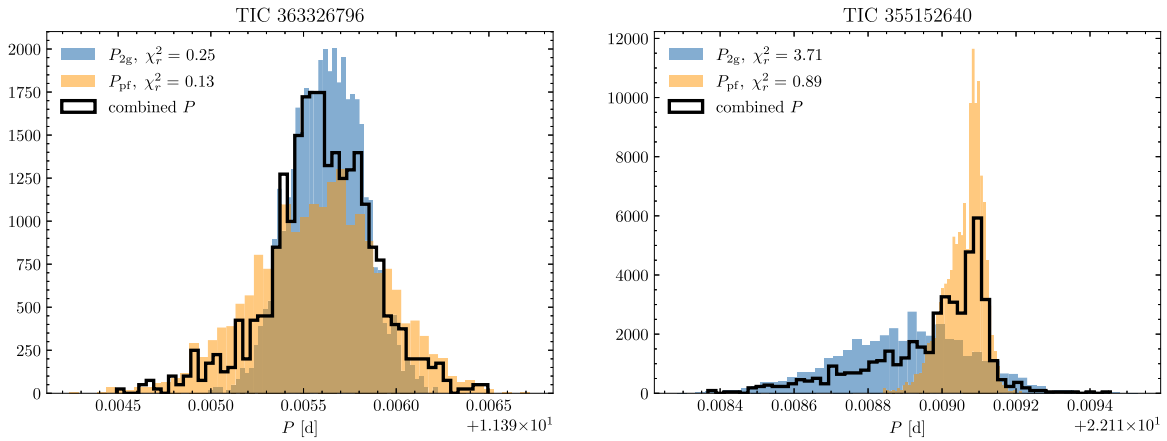


Figure 4. Combined period distribution for a two-Gaussian and polyfit with comparable χ_r^2 (left) and one where polyfit is significantly better (right).

variable in the range $[0,1]$, where 0 corresponds to the widest detached systems and 1 to ellipsoidal variables. We use the Kepler EBs data set to train a neural-network (NN) model on the light-curve geometry and output a value of the morphology parameter. The Kepler and TESS EBs data sets are both preprocessed in the same way: phase-folded with the final catalog ephemerides and binned in 1000 phase bins over the range $[-0.5, 0.5]$. The NN architecture consists of an input layer of size 1000, corresponding to the phased light curves; three dense layers of size 300, 100, and 30, respectively; and an output layer of size 1, corresponding to the morphology parameter. The NN is trained on 60% of the Kepler data set and tested on the remaining 40%, yielding a mean squared error loss of 0.0035.

Figure 5 demonstrates the relationship between the morphology, periods, and primary eclipse widths in the catalog. Long-period systems have morphology parameters close to zero, signaling wide detached binaries, while the shortest period systems tend toward a morphology of 1, which corresponds to contact binaries and ellipsoidal variables. The primary eclipse widths, as determined by the two-Gaussian model, are encoded in the color map, further confirming that the morphology parameter captures the expected variability in eclipse widths: narrow eclipses in systems with a morphology close to 0 and wider eclipses going toward a morphology of 1.

4. EB Validation

Data validation reports, for the purposes of this project, are cumulative accounts of analyses carried out using TESS data for each individual target flagged as an EB. Each report contains, but is not limited to, the full light curve, target parameters, background flux plots, aperture size plots, power spectra, evolutionary tracks, and results from several eclipsing binary data validation tests. The purpose of these validation reports is to support the eclipsing binary classifications of the TESS EB working group.

Eclipsing binary data validation resulted primarily from reformatting the interactive code, LATTE (Light curve Analysis Tool for Transiting Exoplanets; Eisner et al. 2020). LATTE’s initial purpose involved identifying false positives in exoplanet classifications due to instrumentation and astrophysical productions of exoplanet-like signatures. The development of ICED LATTE (Interlacing Code for Eclipsing binary Data validation) redirected the purpose of the analysis tool to validate classifications of TESS EBs and flag the presence of false

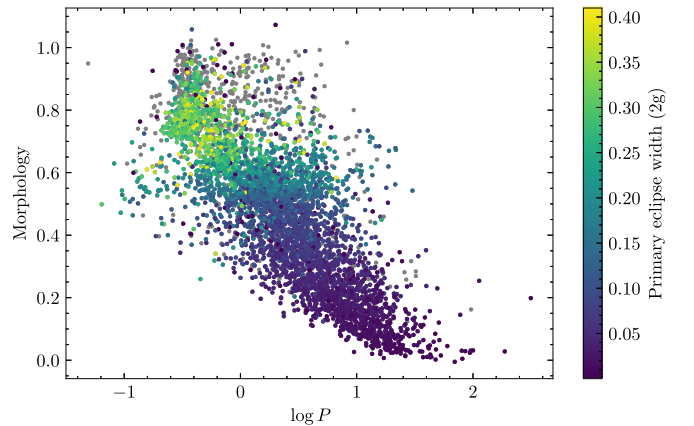


Figure 5. The relationship between morphology parameter, logarithm of the period, and primary eclipse widths, as determined from the two-Gaussian model.

positives. Additionally, LATTE was modified to work without its interactive plots with the aim of producing quick validation reports for the ~ 5000 classified EBs. Additions to ICED LATTE that were not in LATTE include numerous EB validation tests designed to identify whether the signal is on target, tests to determine whether the signal favors the planet or the EB scenario, and a generated likelihood that the target is an EB.

A significant portion of the validation tests are based on light-curve analysis. However, the most telling of the validation tests is based on target pixel file analysis (see Figure 6). The large, $21''$ pixels substantially increase the probability of background contamination from sources other than the TESS target being observed. In the event that an EB is captured in the same aperture as the target, the target itself may appear to be an EB from light-curve analysis. The centroid movement test identifies the presence of other objects in the aperture of the target and measures any movement of the central point of light. If this centroid appears to move slightly between the background object and the target, then one of the two is likely an EB. This is due to the change in flux from the EB. During times of eclipse, the EB appears dimmer and the centroid of light moves toward the stable-flux object. Intuitively, during noneclipse times, the EB appears brighter and the centroid of light moves toward the EB. By analyzing this centroid movement, we are able to determine which of the objects is the true EB and thus confirm or dismiss the EB classification of the TESS target.

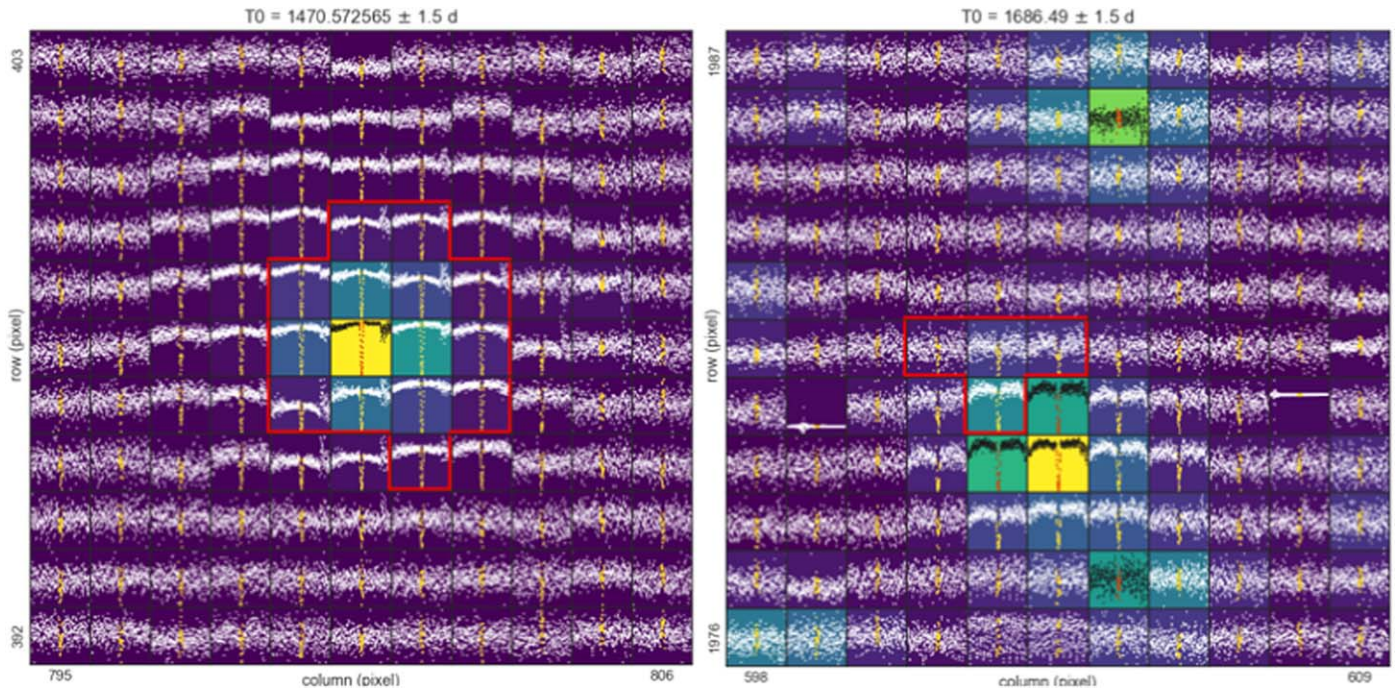


Figure 6. A light curve extracted for each pixel around the target star, where the red line indicates the aperture used to extract the 2 minute cadence SPOC light curve. Left: example of an EB that is on target (TIC 255700967). The overall EB score for this target is 0.87. Right: example of a signal that is not on target (TIC 230530979). The overall EB score for this target is 0.42.

In addition to results from the validation tests, a rough likelihood that the target is an EB is also calculated and included in the data validation report. It should be noted that these likelihoods are extremely general in nature and only reflect the results of the validation tests which are run on the targets. Each test results in a numerical value between 0 and 1; 0 is generally assigned to the test result “Unlikely EB,” 0.5 is generally assigned to “Possible EB,” and 1 is assigned to “Probable EB.” In brief, the validation tests that contribute to this score consist of the following:

1. *Centroid motion.* The centroid test makes use of the open-source python package CONTAMINANTE, which executes a pixel-level modeling of the TESS target pixel files to determine the most likely location of the source of the eclipses. The score for this test is scaled inversely with the distance between the location-calculated source of signal and the location of the target star.
2. *Contamination.* The amount of contamination to the TESS aperture from nearby stars. This provides an indication of how crowded the field is and the likelihood of the signal originating from a nearby companion star. The score for this test is scaled inversely with the contamination of nearby source.
3. *Out-of-transit variability.* EBs with orbital periods shorter than around 3 days are expected to show out-of-transit variability. As such, we search for this variability for the short-period candidates. The significance of such a detection is proportional to the score given for this test. Candidates with periods greater than 3 days are given a score of 0.5 for this test by default.
4. *Archival classification.* Candidates that have previously been listed as an EB on Simbad are awarded a score of 1 while all other candidates are awarded a score of 0.5.

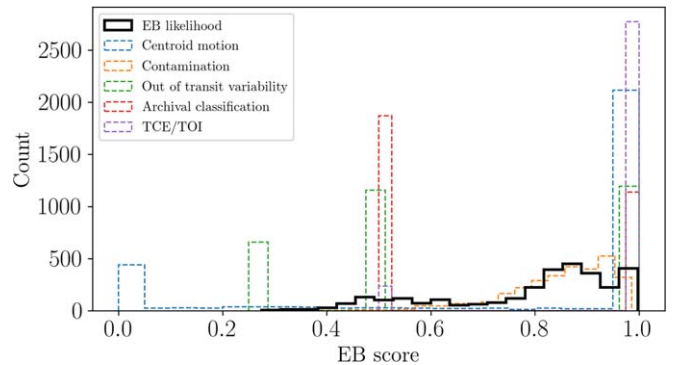


Figure 7. Histogram showing the distribution of the individual test scores (dashed outlines), which combined, give the overall likelihood of the candidate being a real EB (solid black outlines).

5. *TCE/TOI.* The TESS automated search pipeline flags light curves containing a periodic signals, including both planetary and stellar, as threshold-crossing events (TCEs) and TCEs that pass a large number of rigorous planet-vetting tests are promoted to TOI status. As such, candidates that are TOIs are given a score of 0; candidates that are TCEs but not TOIs are given a score of 0.75, and candidates that are neither TOIs nor TCEs receive a score of 0.5.

Due to the large number of signals that are off target, we found the centroid motion test to be the most informative to determine whether the EB signal was real. As such, the final EB likelihood was calculated as the average between all of these test scores, with the centroid motion test given a factor of 3 extra weight. The resulting distribution of the final EB likelihood and of all of the individual test results is shown in Figure 7.

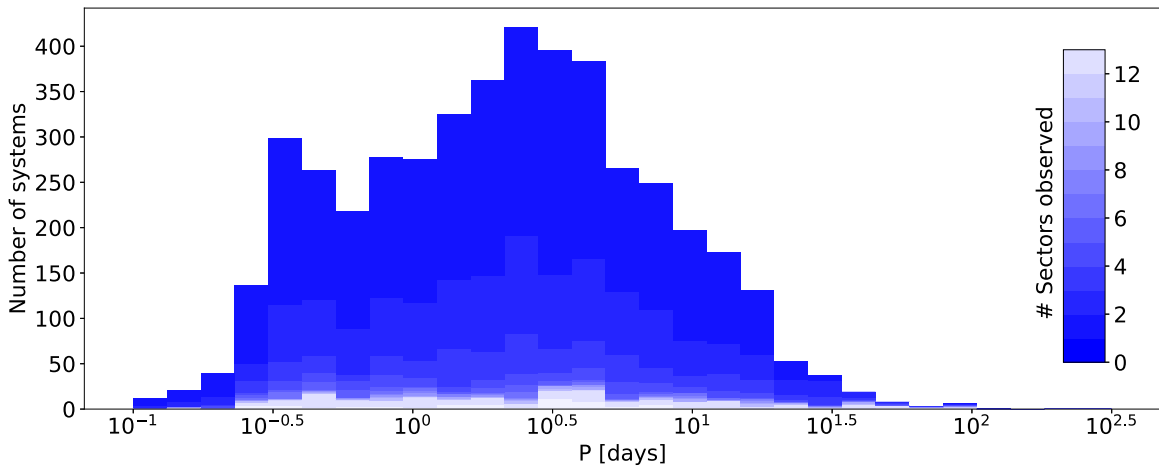


Figure 8. The distribution of orbital periods for 4584 EBs observed in sectors 1 through 26. Shades correspond to the number of sectors in which the target was observed.

5. Statistical Properties of the EB Sample

While nonuniform and magnitude-limited, the sample of 4584 EBs observed by TESS allows us to do preliminary bulk analysis on the data set.

1. *Orbital periods.* The distribution is largely affected by the temporal coverage of observations. Figure 8 shows a bimodal distribution, with a narrow peak at around 0.25 days and a broad peak at around 3 days. The narrow peak corresponds to contact binaries, while the broad peak corresponds to close, detached EBs. We discuss this further in Section 7. The shades of blue correspond to the number of sectors that the targets were observed in; it shows the comparative rates of EBs in the continuous viewing zones (lightest shade) and single sector visits (darkest shade); the histogram is stacked, i.e., the values per bin are cumulative over all sector visits.
2. *Eclipse depths.* Figure 9 depicts their distribution, along with the distribution of eclipse depth ratios. By definition, the primary eclipse depth is deeper, so we expect the distribution to have a longer tail. The systems with shallow primary eclipses and undetectable secondary eclipses enhance the first bin of the primary depth distribution. Depth ratios depend on the surface brightness ratio of the two components, and on eccentricity. Surface brightness itself depends on many second-order effects such as gravity-darkening, limb-darkening, and reflection. Thus, relating eclipse depth ratios to underlying parameters is complicated, but in the broadest sense, the distribution of the depth ratios is aligned with the ratios of effective temperatures. The distribution is bimodal, with a peak at 1, corresponding predominantly⁴² to the equal luminosity class pairs, and broad, near-flat distribution between 0.2 and 0.8, corresponding to evolved components.
3. *Eclipse separations.* Phase-space separations of eclipses are a direct measure of the tangential component of orbital eccentricity, $e \cos \omega$. It is reasonably well determined because eclipse positions could be measured

reliably. Figure 10 depicts their distribution; note that the y scale is logarithmic. The strong peak at 0.5 corresponds to circular orbits, which are expected to dominate the EB population at these relatively short periods.

4. *Eclipse widths.* The least well-determined parameters because of their pronounced sensitivity to the exact points of ingress and egress, it is a measure of the radial component of eccentricity, $e \sin \omega$. Figure 11 depicts their distributions. The differences between the two models, polyfit and two-Gaussian, are most pronounced in eclipse widths; nevertheless, the correlation between the two (bottom panel of Figure 11) shows the expected trend (distribution around $y = x$) with an expected scatter due to eccentricity effects.

5.1. Catalog Completeness

The sample of EBs presented in this paper is inherently nonuniform: mission targets are selected to maximize the exoplanet detection yield and guest investigator targets are selected through proposal competition across a great many science goals. It is thus impossible to use these data to get statistically representative distributions of parameters; we defer that goal until the time when we have a sample of detected and characterized EBs from full-frame images. Thus, when we say “catalog completeness,” we mean the overall EB detection success in the data set of 2 minute cadence target observations. Quantifying completeness properly thus remains beyond the scope of this paper, but we provide qualitative estimates here.

To estimate completeness qualitatively, we start with combined differential photometric precision (CDPP; Gilliland et al. 2011). CDPP is a measure of light-curve variation—the rms noise of the result of filtering the time series with a high-pass Savitzky–Golay filter and then applying a moving average of 0.5 hr. The top panel in Figure 12 shows CDPP as a function of magnitude for Sector 1 observations. The CDPP values are inherent to aperture light, so they are not corrected for crowding. The second panel in Figure 12 provides a statistical estimate of per-target crowding, i.e., the fraction of light in the aperture coming from the target itself. Thus, a value of 1 means that all light is due to the observed target, while a value of, say, 0.6, means that 60% of the light comes from the target and 40% of the light comes from background sources. Thus, to account

⁴² While a surface brightness ratio of ~ 1 can, in principle, be achieved by luminosity ratios $\neq 1$ and, correspondingly, radius ratios $\neq 1$, the majority of the systems where the surface brightness ratio is ~ 1 corresponds to the same luminosity class, i.e., twin stars (see Figure 20).

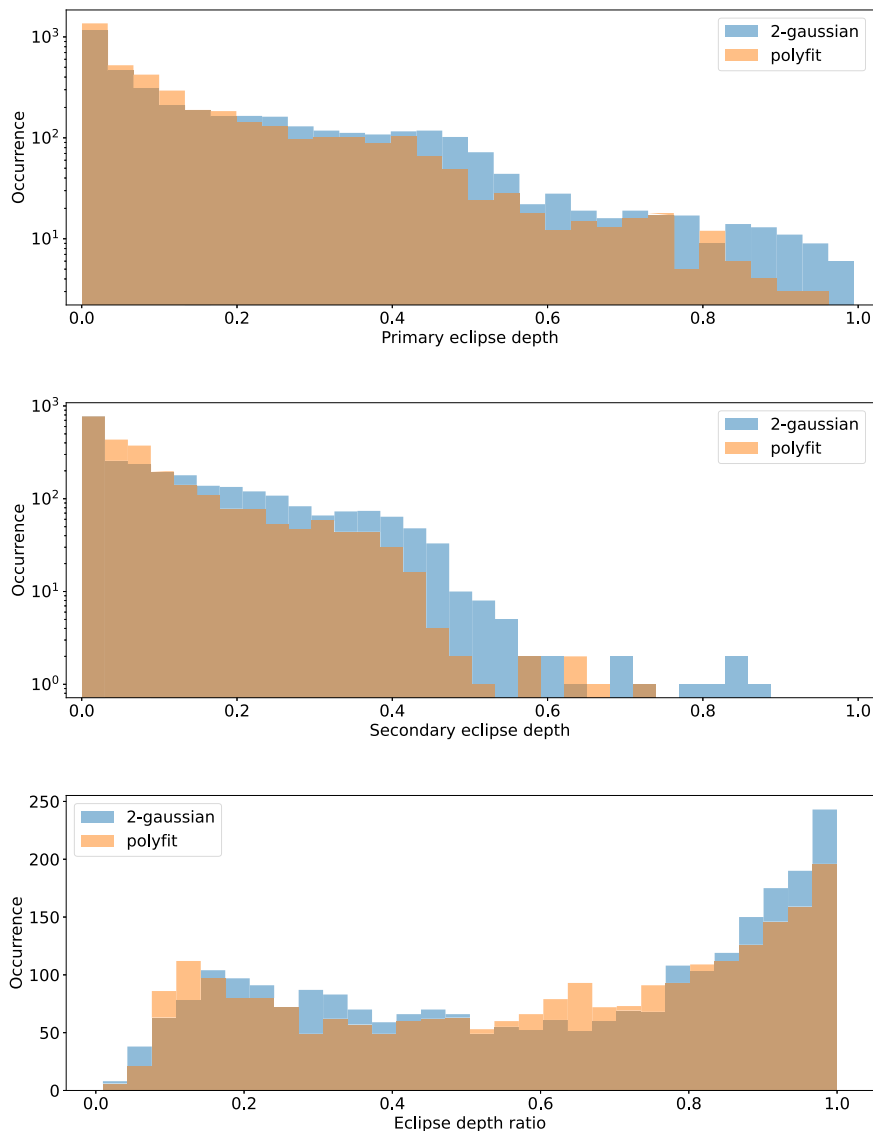


Figure 9. The distributions of primary and secondary eclipse depths and their ratios, derived from the polyfit and two-Gaussian models. Note the log scale of the y-axis. Eclipse depth ratios serve as rough proxies for the surface brightness ratios.

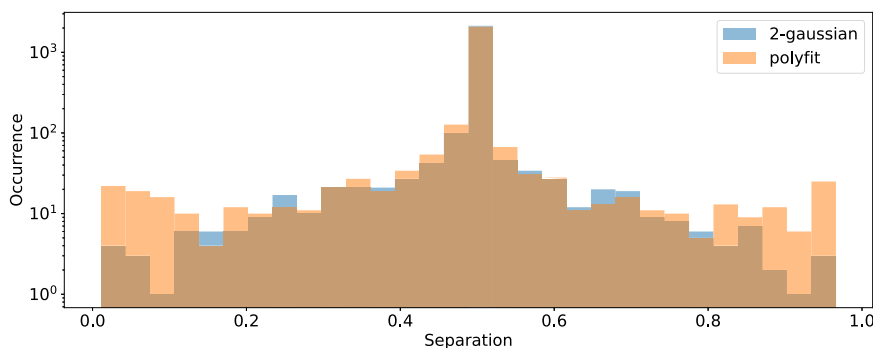


Figure 10. The distribution of eclipse separations in phase space. Eclipse separations serve as proxies for the tangential component of eccentricity, $e \cos \omega$.

for dilution, we correct the CDPF for crowding by dividing it by the crowding factor. This implicitly assumes that the extraneous source of light in the aperture is constant, and that all variability comes from the target itself, which may or may not be true, but overall it plays a small role in correction because crowding is “top-heavy”: 90% of the targets have

crowding factors larger than 0.95. The corrected CDPF is depicted in the third panel of Figure 12. We then fit the bottom envelope by sigma-clipping and divide the corrected CDPF by the envelope in order to flatten out the dependence on magnitude (bottom panel). This way, we can assess the distribution of amplitudes for EBs and its qualitative

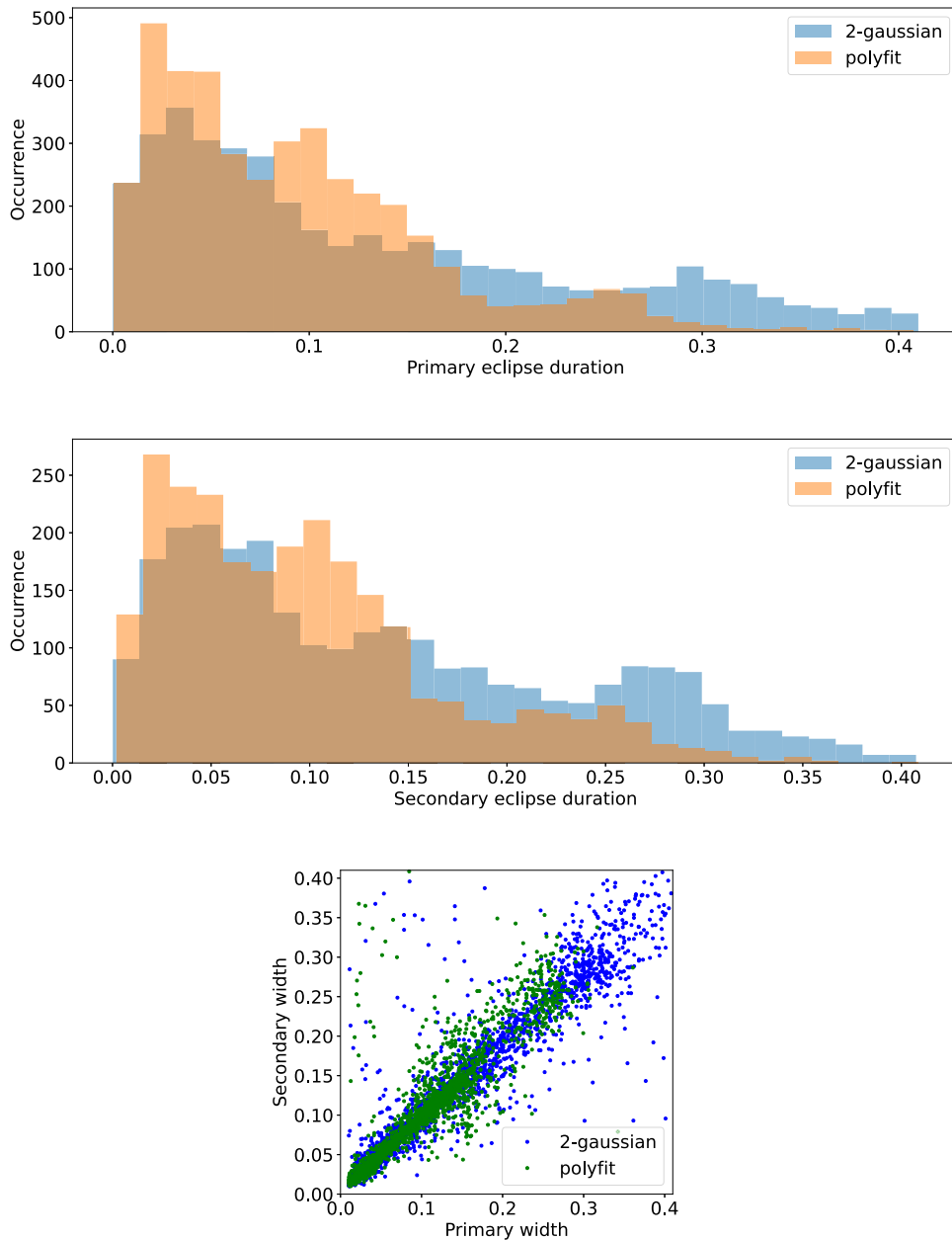


Figure 11. The distributions of primary and secondary eclipse widths, and their correlation, derived from the polyfit and two-Gaussian models. Eclipse widths serve as proxies for the radial component of the eccentricity, $e \sin \omega$.

resemblance to the expected geometric distribution (i.e., the probability of eclipses as a function of orbital elements). We emphasize the word “qualitative” here because, in order to calculate the true geometric distribution, we would need to be able to simulate target list selection, generate a synthetic sample of EBs and, from there, calculate the corresponding CDPP values; this, unfortunately, is not tractable because of the non-prescriptive target selection. The top panel in Figure 13 shows this distribution; we observe a monotonically decreasing trend, in line with expectations. For validation purposes, we check the trend of all targets observed in Sector 1; as we see no systematic features in the flattened CDPP, we conclude that the number distribution is a fair reflection of the true CDPP distribution for the observed EBs.

While not statistically significant, we took a closer look at the slight dip in the fourth bin of the EB distribution; there are

19 EBs out of 299 targets in that bin that were found. We manually went through the entire list of 299 targets again but have failed to find any additional EBs.

Finally, we perform one last check: we test whether the magnitude distribution of EB targets is representative of the overall magnitude distribution; any detected bias might raise completeness questions. Figure 14 demonstrates qualitative equivalence, noting of course that there are no EBs brighter than $T=2.5$, and the diminishing signal-to-noise ratio suppresses eclipse detection on the faint end.

At some level eclipses will blend into the noise background and we will no longer be able to (reliably) detect them; to estimate that level, we take the distribution of primary eclipse depths (see Figure 9) and choose the bin size that yields equal occurrence rates for the first two bins. Phenomenologically that implies that the monotonic increase toward lower S/N stops

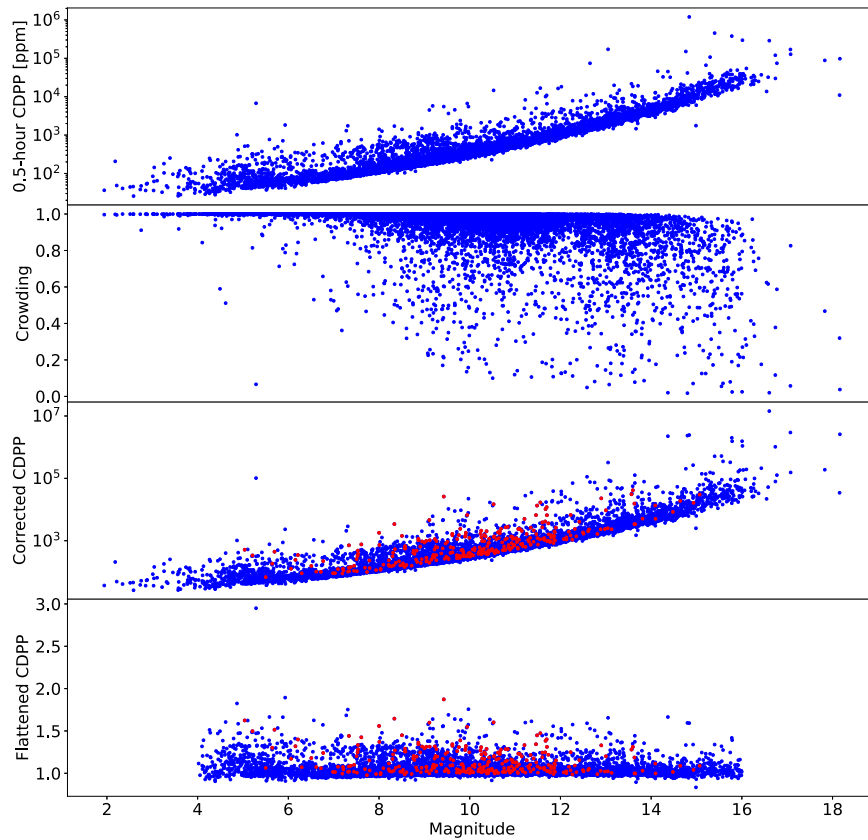


Figure 12. The TESS combined differential photometric precision (CDPP). The top panel depicts the measured CDPP with a 0.5 hr running average, in ppm. The second panel provides a crowding measure per target, i.e., the fraction of light in the aperture from the observed target. The third panel corrects the original CDPP for crowding: corrected CDPP = CDPP/crowding. This assumes that the contribution of background light does not vary with time, which may or may not be true. Depicted in blue are all observed targets, and in red are the EBs. The bottom panel is the flattened version of the previous panel, divided by the bottom envelope.

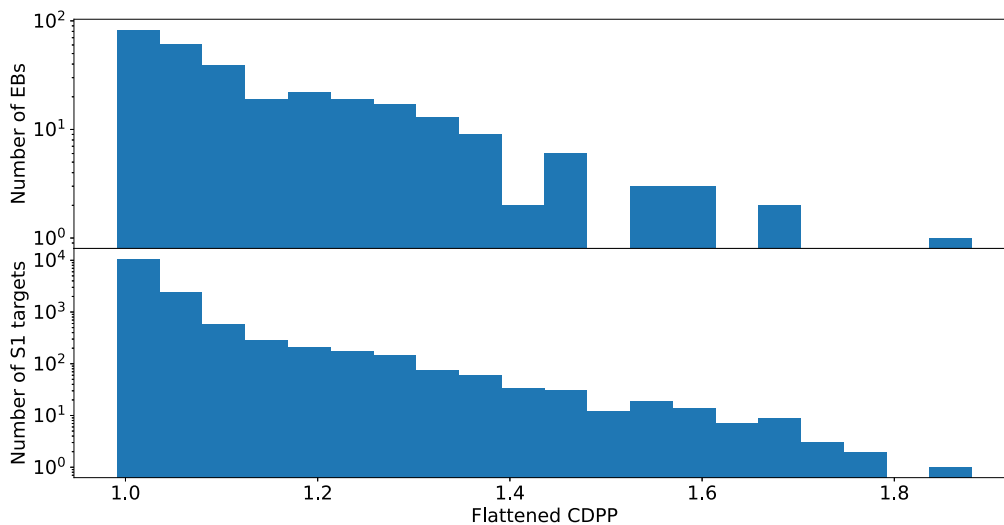


Figure 13. The number of EB targets (top) compared to all Sector 1 targets (bottom) as a function of flattened CDPP. Note the logarithmic y scale.

and that we can no longer reliably detect eclipses. That occurs at $S/N \sim 13$. We take that to be our limit. We conclude that the catalog is largely complete to $S/N \sim 13$.

6. Contents of the Catalog

The TESS eclipsing binary catalog presented here contains all targets observed with a 2 minute cadence in sectors 1

through 26 that are consistent with eclipsing binary signatures. The count as of this writing is 4584 EBs.

All data are available from two official servers: the project’s main webpage, <http://tessEBs.villanova.edu>, and at MAST as a high-level science product via doi:10.17909/t9-9gm4-fx30.⁴³ The official webpage hosts the “rolling” version of the catalog

⁴³ <https://archive.stsci.edu/hlsp/tess-eb>

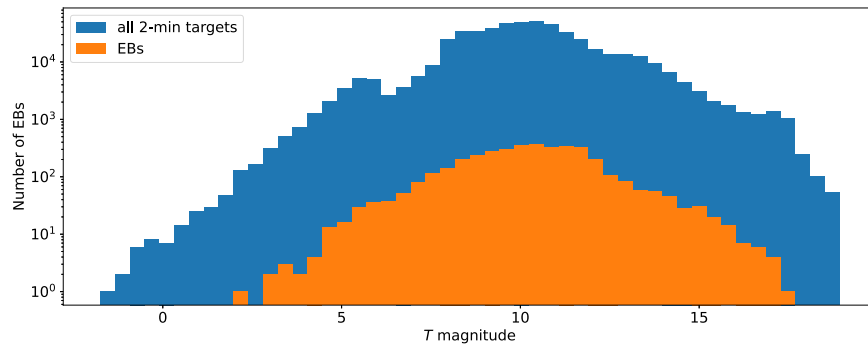


Figure 14. The distribution of TESS magnitudes for all 2 minute targets observed in sectors 1–26 (blue) and all 4584 EBs (amber).

that is updated in real time as new targets are validated or existing targets are refuted. Once every quarter we take a snapshot of the rolling version, tag it with a release number, and deliver it to MAST. Copies of the tagged releases are also kept on the project webpage.

Table 1 summarizes the database tables and columns contained in the catalog along with the relationships between database tables. All entries in the TIC table are copied verbatim from the latest TESS input catalog (v8.1 at the time of this writing; Stassun et al. 2018); all entries in the Sector table are taken from the latest version of the official pointing table⁴⁴; table `Origin` contains identifiers for people or groups who contributed EB candidates (see Section 2). Table `EB` is the central table of the database: it contains links to the TIC, all Sectors the EB is observed in, and all Origins. In addition, it provides the data source⁴⁵ (FFI for full-frame images, TPF for target pixel files, and LCF for light-curve files). It also gives the refined ephemerides (see Section 3.5) and morphology coefficient (see Section 3.6). Table `EphemerisSource` aggregates all automated ephemeris-finding algorithms (see Section 3) and table `Ephemeris` keeps all records on the proposed ephemerides. Note that these are *not* final, refined ephemerides; rather, these are “raw” ephemerides output by the ephemeris-finding algorithms. The `Ephemeris` table also stores triage information: when the triage was done, by whom, what the disposition was, and what proposed ephemerides are likely correct. Finally, the `Comment` table contains all subjective comments made on `Ephemeris`, `EB`, or `TIC` entries.

7. Discussion

In addition to curating information on individual EB targets observed by TESS, the catalog can be used for bulk analysis, similar to what was presented in Section 5. Here we present another two interesting observations.

Figure 15 depicts Galactic latitude distribution of EBs, with two notable features. The first is a near-constant distribution of southern Galactic hemisphere EBs ($-90 < b < -10$), and the second is the lopsidedness between the southern and the northern Galactic hemisphere. The near-constant distribution of EBs is at odds with observations from, say, Kepler (Prša et al. 2011), where Galactic latitude dependence was pronounced. This is a consequence of (1) the nonuniform target selection

presented in Section 2, (2) the relatively bright magnitude breakdown limit for TESS, significantly reducing the dependence of eclipse probability on stellar populations, and (3) the fraction of time the Galactic plane was in or near the CVZ. We expect that EBs detected in FFIs will comprise a more uniform sample that will be more representative of true Galactic distributions of EBs (see Figure 21). The lopsidedness is largely due to the change in boresight in sectors 14–16 and 24–26 (see Figure 1).

The second observation is biased in orbital periods of TESS EBs. Figure 16 (top) shows a comparison between the orbital period distributions for TESS EBs (blue) and Kepler EBs (amber). The long tail for the Kepler sample on the long-period end is expected given that Kepler observed the same field for ~ 4 yr; on the short-period end we see concordance of the narrow peak around $P \sim 0.4$ days between the two data sets, corresponding to contact binary stars, but a different distribution of EBs with periods around 5 days: Kepler’s distribution is mostly flat, while the TESS distribution features a wide peak. This is again a consequence of temporal coverage: the 5 day orbital periods are the sweet spot for TESS with ~ 5 cycles per observed sector, compared to ~ 300 cycles for Kepler. Thus, Kepler’s extended sensitivity toward longer periods means that its detection rates are suppressed almost exclusively by the diminishing geometric probability of eclipses; in contrast, TESS suffers from duty-cycle suppression at orbital periods as short as ~ 13 days, where geometric suppression is not yet dominant. Figure 16 (bottom) depicts a comparison of TESS EBs against the ground-based survey OGLE (green). In this case, we see that the contact binary peak in the OGLE data set is severely enhanced by the diurnal selection effect. Longer periods are significantly suppressed both by the duty-cycle limitations and the geometric probability of eclipses which is now more pronounced because of the sparser, irregular observing cadence. This bias clearly highlights the benefits of space-based surveys such as TESS.

7.1. Goals of the Paper Series

In this first part of the series of papers we presented the sample of 4584 EBs observed by TESS in sectors 1–26. The main science goals that the entire series aims to achieve are as follows:

Study gold-standard EBs. These are known, bright, detached, double-lined binaries with deep eclipses (Torres et al. 2010; Southworth 2015). These are posited to have had minimal interaction histories and have evolved largely independently as single stars. Such systems are considered

⁴⁴ https://tess.mit.edu/wp-content/uploads/orbit_times_20201013_1338.csv

⁴⁵ In this work we only account for the 2 minute cadence LCF observations, but the database allows for adding FFI and TPF data as they are ingested into the catalog.

Table 1
Database Structure of the EB Catalog

Table	Column	Units	Value Type	Description	
TIC:	tess_id	...	long integer	TIC identifier	
	ra	deg	float [0, 360)	R.A.	
	dec	deg	float [−90, 90]	decl. in deg	
	glon	deg	float [0, 360)	Galactic longitude	
	glat	deg	float [−90, 90]	Galactic latitude	
	Tmag	...	float	TESS magnitude	
	teff	K	float	estimated effective temperature	
	logg	log(cgs)	float	estimated surface gravity	
	abun	log(sol)	float	estimated metal abundances	
	pmra	mas/yr	float	proper motion in R.A.	
Sector:	pmdec	mas/yr	float	proper motion in decl.	
	sector_id	...	integer	Sector identifier	
	date_start	iso	date	start date of sector observations	
	date_end	iso	date	end date of sector observations	
	spacecraft_ra	deg	float [0, 360)	satellite R.A.	
	spacecraft_dec	deg	float [−90, 90]	satellite decl.	
	spacecraft_roll	deg	float 0, 360]	satellite roll from reference point	
	cameraN_ra	deg	float [0, 360)	camera N R.A., $N = 1 \dots 4$	
cameraN_dec	deg	float [−90, 90]	camera N decl., $N = 1 \dots 4$		
cameraN_roll	deg	float 0, 360]	camera N roll from reference point, $N = 1 \dots 4$		
Origin:	name	...	string	data/classification origin string	
EB:	tic	...	TIC	link to the TIC entry	
	origin	...	Origin	link to the origin entry	
	sectors	...	Sector	list of sectors the EB was observed in	
	signal_id	...	integer	EB signal enumerator	
	in_catalog	...	boolean	flags the EB as validated	
	date_added	iso	date	time and date of the database entry	
	date_modified	iso	date	time and date of the database modification	
	source	...	choice	data source: ‘FFI’, ‘TPF’ or ‘LCF’	
	bjd0	days	float	BJD−2457000 of the primary eclipse	
	bjd0_uncert	days	float	uncertainty in bjd0	
	period	days	float	orbital period	
	period_uncert	days	float	uncertainty in orbital period	
	morph_coeff	...	float	morphology coefficient	
	morph_dist	...	float	orthogonal distance from the morphology manifold	
	EphemerisSource:	model	...	string	Model used for the ephemeris estimate
		version	...	string	Model version
		author	...	string	Model author
reference		...	string	Model reference	
Ephemeris:	date_added	iso	date	Ephemeris estimate date	
	source	...	EphemerisSource	Ephemeris source	
	eb	...	EB	link to the EB entry	
	bjd0	days	float	BJD−2457000 of the primary eclipse	
	bjd0_uncert	days	float	uncertainty in bjd0	
	period	days	float	orbital period	
	period_uncert	days	float	uncertainty in orbital period	
	triage_timestamp	iso	date	time of performed triage	
	triage_status	...	string	triage disposition	
	triage_period	...	choice	choice of ‘period’, ‘half’, ‘double’, ‘other’	
	triage_username	...	string	person completing the triage	
	Comment:	author	...	string	comment author
		text	...	string	comment text
timestamp		iso	date	comment date and time	
ephem		...	Ephemeris	link to the ephemeris entry	
eb		...	EB	link to the EB entry	
tic		...	TIC	link to the TIC entry	

“gold standards” because they hold promise for the most accurate fundamental parameters. These EBs have spectroscopic data already available and TESS provides us with an improvement in the photometric light-curve quality and temporal coverage.

Estimate photometric elements for all TESS EBs. Eclipsing binary light curves hold a wealth of information about a system and its stellar components. Using PHOEBE and its framework for inverse problem solvers (Conroy et al. 2020), we can estimate photometric parameters of all

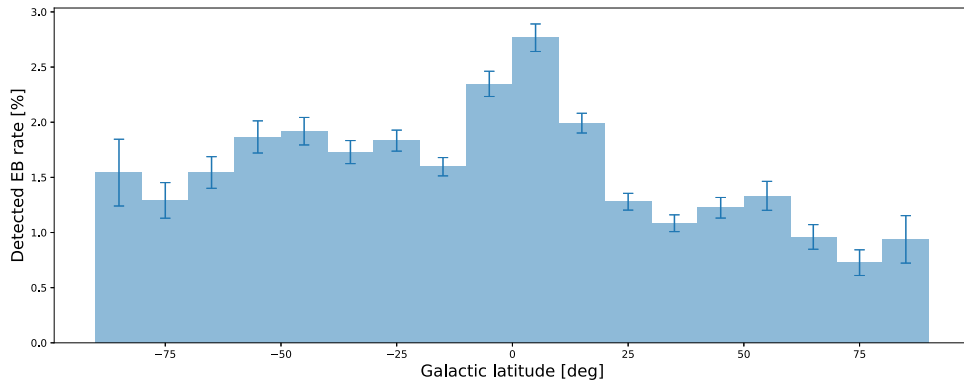


Figure 15. Detection frequency of EBs as a function of Galactic latitude. The frequency is computed by counting all detected 2 minute cadence EBs in a given 10° Galactic latitude strip and dividing the count with the number of all 2 minute cadence targets observed in the same strip.

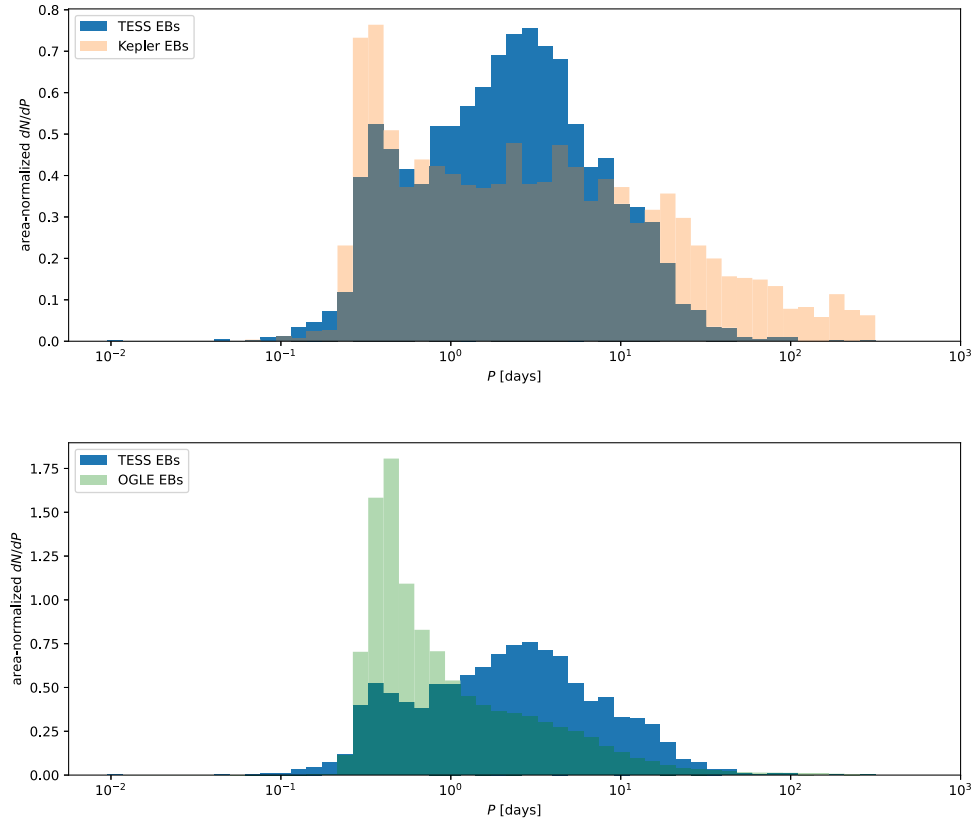


Figure 16. The comparison of orbital period distributions from TESS, Kepler, and OGLE. All distributions are normalized by their surface areas for comparison purposes.

TESS EBs with minimal manual intervention. Using the ephemerides and geometrical estimates from the catalog as a starting point, we can determine the sum and ratio of fractional radii; temperature ratio of the components; the inclination, eccentricity, and argument of periastron of the orbit; and passband luminosities and potential third-light contribution. In addition, for closed systems, the mass ratio and semimajor axis can be constrained from light curves alone (Wilson 1994; Terrell & Wilson 2005). A full Bayesian analysis with MCMC also yields posterior distributions for second-order effects, like the effective temperature of the primary, gravity-darkening coefficients, and albedoes, which, given the photometric precision of TESS, can be used to refine the current empirical laws.

The main perceived impact of this study will be the

period–eccentricity distribution of the TESS EBs sample, which is crucial in studies of binary star populations. In addition, interesting and benchmark systems will be identified for radial-velocity follow-up and more advanced analysis.

Extend the temporal coverage with archival photometry. TESS observations last about 27 days for each sector. Roughly 70% of the sky was observed during the prime mission (Guerrero et al. 2021) and of the 232,705 stars observed at 2 minute cadence, 152,993 ($\sim 66\%$) were observed for just one sector, while the rest were observed in multiple sectors, and 3874 ($\sim 1.7\%$) were observed for 13 consecutive sectors over 351 days. While the observations are not fully continuous, with gaps between orbits and some time lost for engineering or safe modes, in general, a

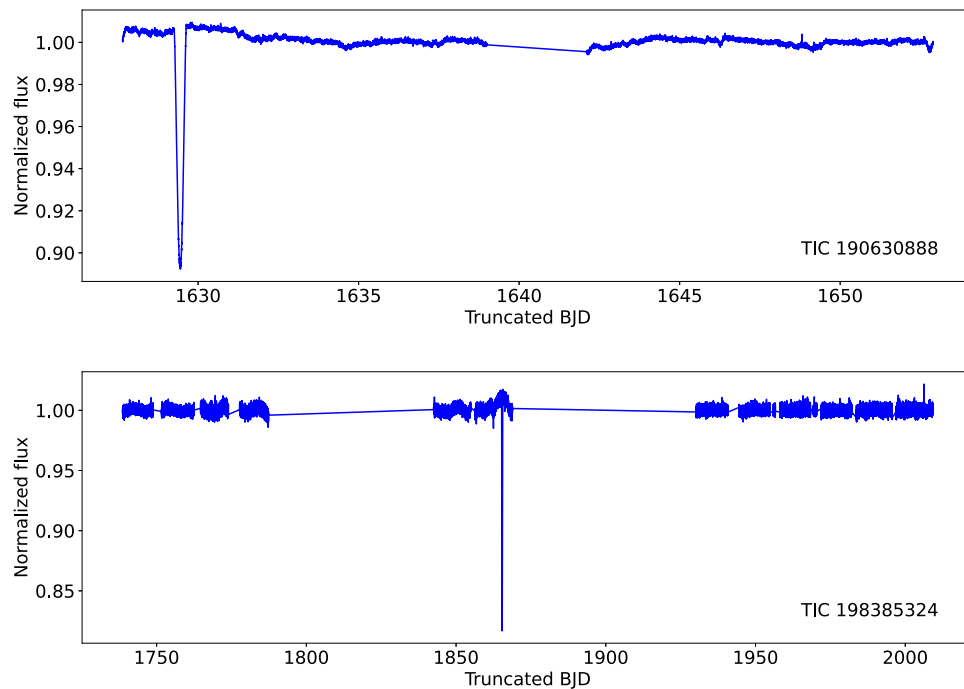


Figure 17. Examples of single-transit EBs, TIC 190630888 and TIC 198385324.

given time baseline of observations means that it is possible to detect EBs with orbital periods up to half the time baseline of observations.

At the long end of that detectability time frame, ambiguities exist in the characterization of the EBs. In some cases, it is not clear whether two distinct eclipses are seen. In others, spot modulation or other variability can interfere with the identification or measurement of an eclipse. For EBs with orbital periods greater than half the observing time baseline, only a single eclipse may be detected, yielding a likely identification of an EB without a reliable period measurement. See examples in Figure 17. For all these reasons, the set of TESS-detected EBs can benefit from cross-identification with other photometric surveys.

A number of such surveys have been conducted and can be combined with TESS observations. Many surveys were carried out to search for transiting exoplanets, including WASP (Pollacco et al. 2006), HAT (Bakos et al. 2004, 2013), KELT (Pepper et al. 2007, 2012), and others⁴⁶ Other surveys have been conducted to search for stellar variability, such as ASAS (Pojmanski 1997), ASAS-SN (Shappee et al. 2014), ATLAS (Tonry et al. 2018), and ZTF (Bellm et al. 2019). While none of these surveys have the photometric precision or cadence of TESS, they all have greater observing time baselines over large fractions of the sky. EBs identified in TESS data with ambiguous ephemerides can be matched to the archival photometric observations to identify eclipses and refine the ephemerides. Such an effort will typically only recover EBs with deep eclipses, but that still represents a large fraction of the EB population. The archival photometry can determine or refine the ephemerides of the EBs and can be used to search for eclipse time variations (ETVs; Conroy et al. 2014) or apsidal motion [REF](Orosz 2015;

Borkovits et al. 2016a; Kirk et al. 2016b). Further development of the TESS EB catalog will incorporate such analysis.

In addition to the use of archival photometry, individual systems of interest can be followed up for astrophysical investigation with modest observing facilities. While broader scientific themes are outlined below, small-telescope observatories are well equipped to observe the bright EBs identified in this catalog. An example of that kind of investigation is multiband photometric follow-up of the O’Connell effect (Milone 1968), in which light curves show unequal maxima before and after the primary eclipse. Follow-up observations in different bandpasses are necessary to understand the underlying cause of this phenomenon. Furthermore, while archival photometry can recover the orbital period for some long-period EBs, as described above, follow-up photometry can readily refine the orbital parameters more precisely.

Study asteroseismic components in EBs. The exquisite precision, cadence, and duty cycle of TESS observations have revealed resolved pulsations in stars across all spectral types and evolutionary phases (Antoci et al. 2019; Pedersen et al. 2019; Córscico et al. 2021). Given the ubiquity of both stellar pulsations and stellar multiplicity, binary systems with at least one pulsating component are commonly found. The complementary nature of asteroseismic (interior) and binary (bulk) information enables highly detailed evolutionary modeling. Such synergistic combined modeling approaches have led to detailed inference on the structure of stars from solar-like oscillators to massive β -Cep pulsators to evolved stars that have undergone mass transfer (De Cat et al. 2004; Guo et al. 2016; Schmid & Aerts 2016; Guo et al. 2017; White et al. 2017; Beck et al. 2018; Streamer et al. 2018; Johnston et al. 2019, 2021). Furthermore, detailed studies have demonstrated tension between the asteroseismic and binary results for both main sequence and evolved stars,

⁴⁶ See Deeg & Alonso (2018) for a larger list.

indicating that evolutionary models still have room for improvement (Gaulme et al. 2016; Themeßl et al. 2018; Benbakoura et al. 2021; Sekaran et al. 2021). The large data set provided by TESS will enable synergistic asteroseismic and binary modeling across a much larger parameter range than was previously possible with the more limited samples, allowing investigation into the relationship between pulsational properties and orbital properties (Liakos & Niarchos 2017; Gaulme & Guzik 2019; Sekaran et al. 2020).

Ground-based radial-velocity follow-up of binary systems is time-consuming, resource-intensive, and simply expensive. Due to their stability over long time bases, heat-driven pulsations act as regular clocks, whose phase (and frequency) is modulated due to the light-travel-time effect from the orbital motion. By measuring the observed phases of pulsations across the orbit, one can reliably derive the radial-velocity curve of the pulsating component from the photometry alone (Shibahashi & Kurtz 2012; Murphy et al. 2014; Hey et al. 2020). The application of this method to this database (where appropriate, given the ratio of pulsation period to orbital period) can produce a wealth of radial-velocity curves without needing to apply for costly ground-based telescope time.

Explore the impact of dynamical tides. Kepler discovered 172 heartbeat stars (HBs), and about one fifth show tidally excited oscillations (Kirk et al. 2016a; Guo et al. 2020), i.e., the direct manifestation of dynamical tides. A handful of them have been studied in detail (Welsh et al. 2011; Hambleton et al. 2013, 2016, 2018; Shporer et al. 2016; Fuller et al. 2017; Guo et al. 2017, 2019). Recently, Guo (2021) reviewed the current status of heartbeat binaries with tidally excited oscillations. Most Kepler HBs are of A–F types due to selection biases. TESS is destined to discover more massive O–B type heartbeat binaries. Systems already published include Jayasinghe et al. (2019, 2021) and Kołaczek-Szymański et al. (2021). To date, we have identified 25 HB systems in the 2 minute TESS data up to Sector 26, and over 200 systems in the 2 minute and FFI data combined. Given that 5% of the binary stars in the Kepler catalog with periods less than 27.3 days (the length of a TESS sector) were classified as heartbeat stars, we anticipate that the number we have identified is a lower limit.

The advent of the TESS mission has also revealed a new class of pulsating stars in binaries, wherein the pulsation axis is “tidally tilted,” producing a characteristic amplitude and phase modulation (Fuller et al. 2020; Handler et al. 2020; Kurtz et al. 2020; Rappaport et al. 2021). Additionally, a few studies have reported the detection of so-called “tidally perturbed” pulsations, where a series of pulsations that are nearly equidistantly spaced by the orbital frequency were detected (Bowman et al. 2019; Southworth et al. 2020; Steindl et al. 2021). Such systems cannot currently be explained by the same model as the “tidally tilted” pulsators, and seem to have a separate connection to the interplay between tides and pulsations. While only a handful of these objects have been identified to date, they signify a unique contribution of TESS to the progress of tidal asteroseismology. The compilation of this database serves to streamline the detection of even more systems.

Stellar multiples and circumbinary planets. A large number of eclipsing binaries have third-body companions that are detected via eclipse timing variations (ETVs), either light-travel-time effects (LTTE, the most common) or dynamical effect delays. A fraction of these exhibit tertiary eclipses as well. For example, Borkovits et al. (2016b) found good evidence for third bodies in 222 eclipsing binaries out of 2600 studied using Kepler data. In most cases, the ETV signal becomes significant on timescales similar to or longer than the period of the outer orbit, which is typically a few to several hundred days for the systems found by Borkovits et al. (2016b).

Rather than being a star, in some cases, the third body is a planet—a so-called circumbinary planet. Kepler revealed 13 such planets that transited their host stars (e.g., see Doyle et al. (2011), Welsh et al. (2012), Orosz et al. (2019)). While few in number, these systems provide a great deal of information, e.g., extremely accurate (not just precise) stellar parameters and planetary radii. But with only a handful of systems, we cannot understand the characteristics of the population of circumbinary planets. TESS’s all-sky survey could remedy this small sample-size problem, but for most of the sky, only ~ 27 days of near-continuous coverage per two years is available and this window is much shorter than the typical circumbinary planet orbital period. Fortunately, the duty cycle at the ecliptic poles is much better and the first TESS circumbinary planet, TOI-1338 (Kostov et al. 2020a), was detected in observation from TESS’s continuous viewing zone (CVZ) at the southern ecliptic cap. In addition to the long-duration observations at the CVZ, we can search for circumbinary planets by taking advantage of the extra information provided when the planet transits both stars in the binary. Unlike a planet orbiting a single star, a circumbinary planet can produce two, and possibly more, transits during one conjunction’s pass. This “1–2 punch” technique (Jenkins et al. 1996; Kostov et al. 2020b) was used to detect the second TESS circumbinary planet, TIC 172900988 (Kostov et al. 2021a). Roughly 140 ± 110 new circumbinary planets may potentially be found via this technique, in addition to the 40 ± 32 expected in the two CVZs (Kostov et al. 2020b). Thus TESS should be able to boost the number of circumbinary planets by an order of magnitude, allowing a much more robust estimate of the occurrence rate, population statistics, and searches for correlation with various binary star parameters (e.g., metallicity, eccentricity, mass ratio, etc.).

Gaia data overlap. Of the 4584 EBs in the catalog, a total of 4550 have entries in the early third data release of the Gaia catalog (Gaia EDR3; Gaia Collaboration et al. 2021). The top three panels in Figure 18 show histograms of the G -band magnitudes and the $G_{BP} - G_{RP}$ colors for the combined light of each binary and of their distances, where the latter are derived here simply as the reciprocal of the trigonometric parallax (see Bailer-Jones et al. 2021). The distribution of magnitudes up to about $G = 12$ largely reflects the content of the TIC candidate target list, while the fainter stars are special interest targets that come from the Guest Investigator Program. The typical color index is very near solar. As expected from their brightness, most of these objects are relatively nearby, with the peak of the distribution located at ~ 150 pc, and a long tail toward

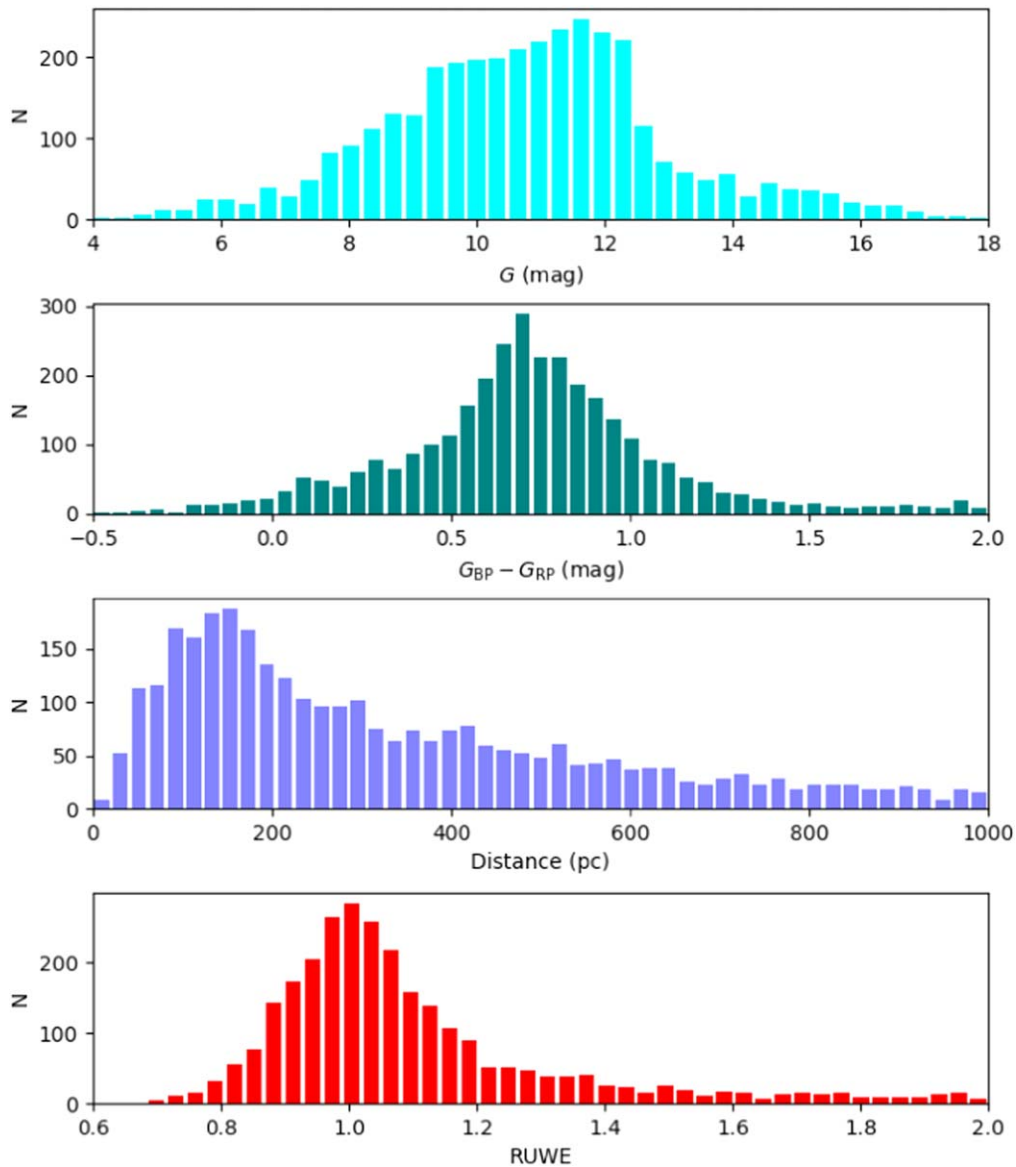


Figure 18. Distributions of the Gaia EDR3 brightness, color, distance, and RUWE for the eclipsing binaries in the catalog. The histograms are truncated on the right (and some on the left) for clarity.

larger distances (truncated in the figure).

The bottom panel displays the distribution of the renormalized unit weight error (RUWE) from Gaia, which is regarded as a useful measure of the quality and reliability of the astrometric solution⁴⁷. RUWE values for well-behaved solutions cluster around 1.0, whereas values larger than about 1.4 typically indicate unmodeled excess scatter in the astrometric observations that can be caused, e.g., by binarity of the source or perhaps other effects. Gaia does not spatially resolve any of the EBs in this catalog; it only measures the center of light. In many cases, the binary motion will cause the flux centroid to wobble enough to be detected by Gaia, perturbing the astrometric solution.

Stassun & Torres (2021) have shown that even in the 1.0–1.4 range the RUWE values tend to correlate with the

semimajor axis of the photocentric motion. For the binaries in the catalog, we do not have sufficient information to estimate the semimajor axis of the photocenter. However, we can place the EB sample into the broader context of typical RUWE values for Gaia stars across the HR diagram. This is shown in Figure 19, where the left panel represents the RUWE in grayscale for the ~ 1 million Gaia EDR3 stars within 400 pc having $5 < G < 19$ and $|b| > 60^\circ$, and the right panel overlays in green the EB sample. In both panels, a piecewise linear fit is shown over the “spine” of the single-star main sequence, for which the RUWE values are at a minimum (dark gray). Various populations with relatively high binary star fractions appear above and below the single-star main sequence (lighter shades of gray), as described in detail by Belokurov et al. (2020).

Relative to the single-star main sequence, the EBs identified in this paper are in almost all cases displaced upward/redward, as expected for the combined light of

⁴⁷ See the report by L. Lindgren in the Gaia documentation, <https://www.cosmos.esa.int/web/gaia/public-dpac-documents>.

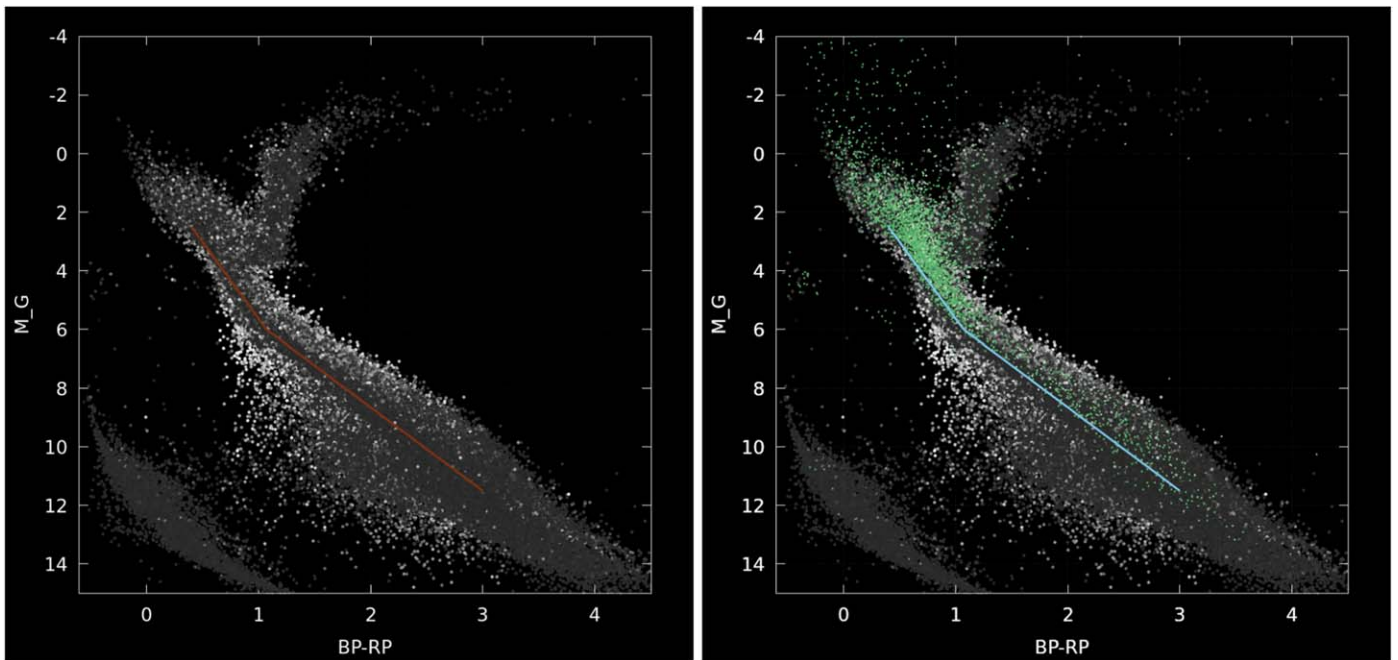


Figure 19. The color–magnitude diagram in the Gaia passbands. The grayscale denotes the renormalized unit weight error (RUWE) parameter for ~ 1 million Gaia EDR3 targets within ~ 400 pc. Left: Gaia-only targets, with the piecewise linear line showing the fit to the lowest RUWE values. Right: TESS EBs plotted over Gaia targets; most EBs are displaced to the brighter, redder region of the CMD.

pairs of stars having various relative luminosities and colors. And relative to the minimal RUWE values typical of the single-star main sequence, the EBs occupy regions that are characterized by higher RUWE values on average.

We can also use the recent work of Belokurov et al. (2020) to assess the likely nature and evolutionary states of the EBs. In Figure 20, we represent the EB sample in the color–magnitude diagram with theoretical evolutionary tracks overlaid to provide a sense of the mass range of the systems, as well as boxes with annotations indicating EBs in evolutionary states that may be of particular interest for various astrophysical applications (see, for example, the work on extreme horizontal branch stars by Sahoo et al. 2020 and Baran et al. 2021).

Finally, it is now well established that short-period binary stars are very frequently found in hierarchical triple systems, with a tertiary companion on a much larger orbit around the tight binary (see, e.g., Tokovinin et al. 2006; Laos et al. 2020, and references therein). We cross-matched our EB sample with the catalog of wide binaries in Gaia EDR3 from El-Badry et al. (2021), to assess if any of the EBs are in fact members of hierarchical triples.

We cross-matched our EB sample with the catalog of wide binaries in Gaia EDR3 from El-Badry et al. (2021), to assess if any of the EBs are in fact members of hierarchical triples. This yielded 711 wide binary candidates in which at least one component is in our TESS EB sample. Of these, 665 have greater than 90% probability of being gravitationally bound ($R_{\text{chance}} < 0.1$). The TESS EB is the brighter (fainter) component in 632 (64) of the high-probability binaries. Thirty-one high-probability binaries have *both* components in our TESS EB sample. We defer further analysis of this sample to future work.

Use calibrated 2 minute cadence targets for FFI extraction. There are several community-led projects that focus on light-curve extraction from TESS FFIs. The tools and the

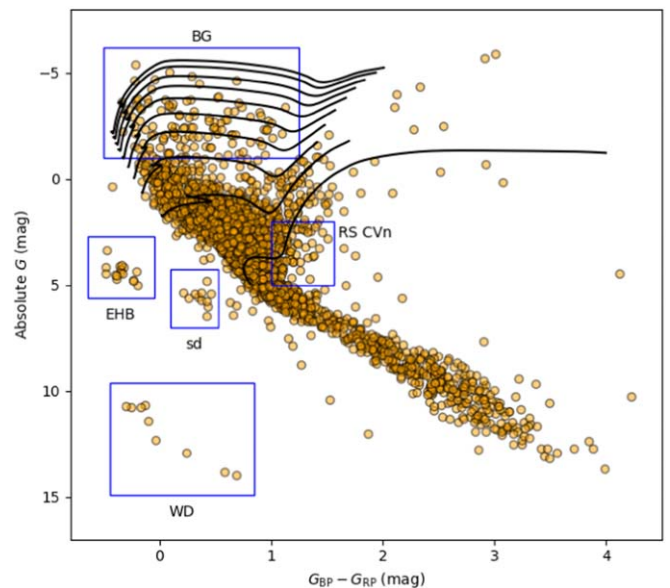


Figure 20. EB sample in the color–magnitude diagram with theoretical evolutionary tracks spanning 1–10 solar masses and boxes indicating evolutionary states of particular interest (see, e.g., Belokurov et al. 2020), including white dwarfs (WD), hot subdwarfs (sd), extreme horizontal branch (EHB) stars, RS CVn systems, and a remarkably large number of bright giants (BGs; i.e., giant stars of intermediate mass).

data products stemming from those projects have been released to the public; we base our extractions on an adapted version of *eleanor* (Feinstein et al. 2019). We use the EBs observed with the 2 minute cadence as the training set for the back-propagating neural network that will sift through all FFI light curves and find those that resemble EBs. The amount of cyan in Figure 1 clearly showcases why manual vetting is *not* tractable and why we *must* resort to automated techniques. We will extract FFI

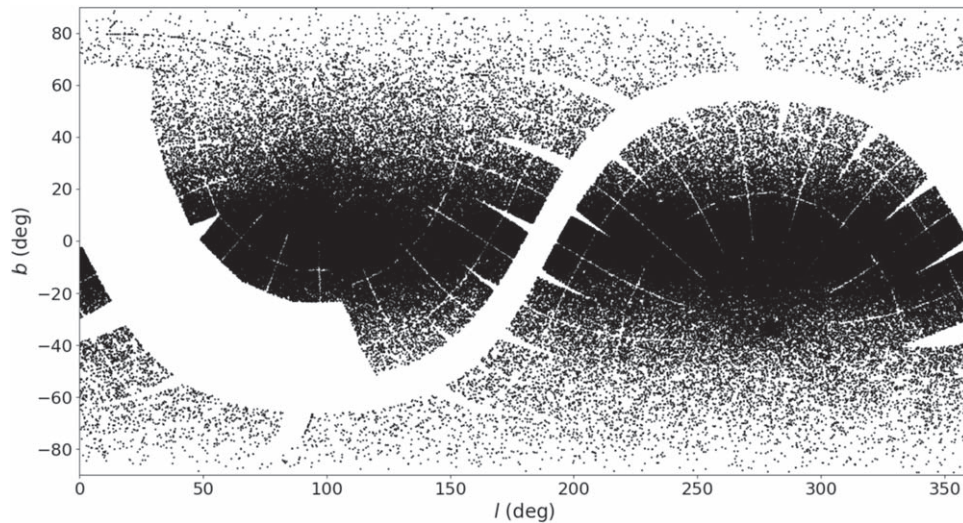


Figure 21. Galactic coordinates of each of the 460,000+ EB candidates found using a neural network on all TESS light curves up to 15th magnitude in sectors 1–26.

light curves for each of the 2 minute cadence EBs, formulate a fidelity metric based on the comparison between FFI-extracted and 2 minutes cadence light curves that can be inspected manually, train a classifying, back-propagating neural network on the FFI-extracted light curves of the 2 minute cadence EBs, and deploy the network on *all* FFI light curves to automatically detect EBs lurking in the images.

Analyze contents of a catalog of EBs extracted from the FFIs. Several of our co-authors have constructed all light curves from TESS FFIs up to 15th magnitude, resulting in more than 72 million light curves from sectors 1–26. The authors constructed a one-dimensional convolutional neural network, first described in Powell et al. (2021), to extract candidate EBs from these light curves, resulting in a catalog of over 460,000 sources, of which we expect 250,000 to be true sources (i.e., not due to light-curve contamination). The coordinates of these candidates are shown in Figure 21. Among these candidates were found several interesting multiple-star systems (Kostov et al. 2021b; Powell et al. 2021), with many others currently being researched. The greatest value of this effort, however, may indeed lie in the use of the full catalog of candidates. Cross matching with other catalogs could identify higher-order multiples or binaries containing particular stellar types. Statistical analysis of the catalog could also provide tremendous insight into the growing field of EB research.

The catalog of EBs observed by TESS in short cadence is thus only the first step in the exploration of the physical, dynamical, and statistical properties of EBs across the entire sky. The catalog will continue to be updated with new sectors of data as they become available and it will be broadened to include all EB sources detected in the TESS full-frame images. For the latest version of the catalog, please refer to <http://tessEBs.villanova.edu>.













This paper makes use of data collected by the TESS mission, which are publicly available from the Mikulski Archive for Space Telescopes (MAST). Funding for the TESS mission is provided by NASA’s Science Mission directorate. We acknowledge the use of public TESS data from pipelines at



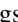

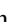


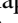






the TESS Science Office and at the TESS Science Processing Operations Center. Resources supporting this work were provided by the NASA High-End Computing (HEC) Program through the NASA Advanced Supercomputing (NAS) Division at Ames Research Center for the production of the SPOC data products.

A.P. acknowledges support from NASA TESS GI programs 18-TESS2-19-0032 and 20-TESS20-0024. L.I.J. acknowledges funding from the European Research Council (ERC) under the European Union’s Horizon 2020 research and innovation program (grant agreement No. 670519: MAMSIE) and from the Research Foundation Flanders (FWO) under grant agreement 1124321N (Aspirant Fellowship). C.J. has received funding from NOVA, the European Research Council under the European Union’s Horizon 2020 research and innovation program (No. 670519: MAMSIE), and from the Research Foundation Flanders under grant agreement G0A2917N (BlackGEM). K.H. would like to thank NASA for their continued support through NASA ADAP program 80NSSC19K0594. We sincerely thank Kareem El-Badry for his help in comparing our catalog with his Gaia Wide Binary catalog.

This work makes use of Python (Python Software Foundation. Available at www.python.org) and the Python packages Django (Django Software Foundation 2020), Numpy (Harris et al. 2020), Numba (Lam et al. 2015), Scipy (Virtanen et al. 2020), and Matplotlib (Hunter 2007).

ORCID iDs

Andrej Prša  <https://orcid.org/0000-0002-1913-0281>
 Angela Kochoska  <https://orcid.org/0000-0002-9739-8371>
 Kyle E. Conroy  <https://orcid.org/0000-0002-5442-8550>
 Nora Eisner  <https://orcid.org/0000-0002-9138-9028>
 Daniel R. Hey  <https://orcid.org/0000-0003-3244-5357>
 Ethan Kruse  <https://orcid.org/0000-0002-0493-1342>
 Scott W. Fleming  <https://orcid.org/0000-0003-0556-027X>
 Martti H. Kristiansen  <https://orcid.org/0000-0002-2607-138X>
 Daryll LaCourse  <https://orcid.org/0000-0002-8527-2114>
 Joshua Pepper  <https://orcid.org/0000-0002-3827-8417>
 Keivan G. Stassun  <https://orcid.org/0000-0002-3481-9052>
 Guillermo Torres  <https://orcid.org/0000-0002-5286-0251>

Michael Abdul-Masih  <https://orcid.org/0000-0001-6566-7568>
 Zhao Guo  <https://orcid.org/0000-0002-0951-2171>
 Kelly Hambleton  <https://orcid.org/0000-0001-5473-856X>
 Kyeongsoo Hong  <https://orcid.org/0000-0002-8692-2588>
 Thomas Jacobs  <https://orcid.org/0000-0003-3988-3245>
 David Jones  <https://orcid.org/0000-0001-9786-1031>
 Veselin Kostov  <https://orcid.org/0000-0001-9786-1031>
 Jae Woo Lee  <https://orcid.org/0000-0002-5739-9804>
 Jerome A. Orosz  <https://orcid.org/0000-0001-9647-2886>
 Brian P. Powell  <https://orcid.org/0000-0003-0501-2636>
 Saul Rappaport  <https://orcid.org/0000-0003-3182-5569>
 Phill Reed  <https://orcid.org/0000-0002-5005-1215>
 Hans Martin Schwengeler  <https://orcid.org/0000-0002-1637-2189>
 Avi Shporer  <https://orcid.org/0000-0002-1836-3120>
 Andrew Vanderburg  <https://orcid.org/0000-0001-7246-5438>
 William F. Welsh  <https://orcid.org/0000-0003-2381-5301>
 Douglas A. Caldwell  <https://orcid.org/0000-0003-1963-9616>
 John P. Doty  <https://orcid.org/0000-0003-2996-8421>
 Jon M. Jenkins  <https://orcid.org/0000-0002-4715-9460>
 David W. Latham  <https://orcid.org/0000-0001-9911-7388>
 George R. Ricker  <https://orcid.org/0000-0003-2058-6662>
 Joshua E. Schlieder  <https://orcid.org/0000-0001-5347-7062>
 Roland Vanderspek  <https://orcid.org/0000-0001-6763-6562>
 Joshua N. Winn  <https://orcid.org/0000-0002-4265-047X>

References

- Antoci, V., Cunha, M. S., Bowman, D. M., et al. 2019, *MNRAS*, 490, 4040
 Astropy Collaboration, Robitaille, T. P., Tollerud, E. J., et al. 2013, *A&A*, 558, A33
 Bailer-Jones, C. A. L., Rybizki, J., Fousneau, M., Demleitner, M., & Andrae, R. 2021, *AJ*, 161, 147
 Bakos, G. Á., Csabry, Z., Penev, K., et al. 2013, *PASP*, 125, 154
 Bakos, G., Noyes, R. W., Kovács, G., et al. 2004, *PASP*, 116, 266
 Baran, A. S., Sahoo, S. K., Sanjayan, S., & Ostrowski, J. 2021, *MNRAS*, 503, 3828
 Barentsen, G., Hedges, C., Vinícius, Z., et al. 2019, KeplerGO/Lightkurve: Lightkurve v1.1.1, Zenodo, doi:10.5281/zenodo.3371790
 Beck, P. G., Mathis, S., Gallet, F., et al. 2018, *MNRAS*, 479, L123
 Bell, E. C., Kulkarni, S. R., Graham, M. J., et al. 2019, *PASP*, 131, 018002
 Belokurov, V., Penoyre, Z., Oh, S., et al. 2020, *MNRAS*, 496, 1922
 Benbakoura, M., Gaulme, P., McKeever, J., et al. 2021, *A&A*, 648, A113
 Bisikalo, D. 2010, in ASP Conf. Ser., 435, Binaries—Key to Comprehension of the Universe, ed. A. Prša & M. Zejda (San Francisco, CA: ASP), 287
 Borkovits, T., Hajdu, T., Sztakovics, J., et al. 2016a, *MNRAS*, 455, 4136
 Borkovits, T., Hajdu, T., Sztakovics, J., et al. 2016b, *MNRAS*, 455, 4136
 Bowman, D. M., Johnston, C., Tkachenko, A., et al. 2019, *ApJL*, 883, L26
 Carter, J. A., & Agol, E. 2013, *ApJ*, 765, 132
 Chakraborty, J., Wheeler, A., & Kipping, D. 2020, *MNRAS*, 499, 4011
 Conroy, K. E., Kochoska, A., Hey, D., et al. 2020, *ApJS*, 250, 34
 Conroy, K. E., Prša, A., Stassun, K. G., et al. 2014, *AJ*, 147, 45
 Córscico, A. H., Uzunoglu, M., Kepler, S. O., et al. 2021, *A&A*, 645, A117
 De Cat, P., De Ridder, J., Hensberge, H., & Ilijic, S. 2004, in ASP Conf. Ser., 318, Spectroscopically and Spatially Resolving the Components of the Close Binary Stars, ed. R. W. Hilditch, H. Hensberge, & K. Pavlovski (San Francisco, CA: ASP), 338
 Deeg, H. J., & Alonso, R. 2018, Handbook of Exoplanets (Berlin: Springer), 117
 Django Software Foundation 2020, Django, v3.0.4, <https://djangoproject.com>
 Doyle, L. R., Carter, J. A., Fabrycky, D. C., et al. 2011, *Sci*, 333, 1602
 Duchêne, G., & Kraus, A. 2013, *ARA&A*, 51, 269
 Eisner, N., Lintott, C., & Aigrain, S. 2020, *JOSS*, 5, 2101
 Eisner, N. L., Barragán, O., Lintott, C., et al. 2021, *MNRAS*, 501, 4669
 El-Badry, K., Rix, H.-W., & Heintz, T. M. 2021, *MNRAS*, 506, 2269
 Feinstein, A. D., Montet, B. T., Foreman-Mackey, D., et al. 2019, *PASP*, 131, 094502
 Foreman-Mackey, D., Farr, W., Sinha, M., et al. 2019, *JOSS*, 4, 1864
 Fuller, J., Hambleton, K., Shporer, A., Isaacson, H., & Thompson, S. 2017, *MNRAS*, 472, L25
 Fuller, J., Kurtz, D. W., Handler, G., & Rappaport, S. 2020, *MNRAS*, 498, 5730
 Gaia Collaboration, Brown, A. G. A., Vallenari, A., et al. 2021, *A&A*, 649, A1
 Gaulme, P., & Guzik, J. A. 2019, *A&A*, 630, A106
 Gaulme, P., McKeever, J., Jackiewicz, J., et al. 2016, *ApJ*, 832, 121
 Gilliland, R. L., Chaplin, W. J., Dunham, E. W., et al. 2011, *ApJS*, 197, 6
 Guerrero, N. M., Seager, S., Huang, C. X., et al. 2021, *ApJS*, 254, 39
 Guo, Z. 2021, *FrASS*, 8, 67
 Guo, Z., Fuller, J., Shporer, A., et al. 2019, *ApJ*, 885, 46
 Guo, Z., Gies, D. R., & Matson, R. A. 2017, *ApJ*, 851, 39
 Guo, Z., Gies, D. R., Matson, R. A., & García Hernández, A. 2016, *ApJ*, 826, 69
 Guo, Z., Shporer, A., Hambleton, K., & Isaacson, H. 2020, *ApJ*, 888, 95
 Hambleton, K., Fuller, J., Thompson, S., et al. 2018, *MNRAS*, 473, 5165
 Hambleton, K., Kurtz, D. W., Prša, A., et al. 2016, *MNRAS*, 463, 1199
 Hambleton, K. M., Kurtz, D. W., Prša, A., et al. 2013, *MNRAS*, 434, 925
 Handler, G., Kurtz, D. W., Rappaport, S. A., et al. 2020, *NatAs*, 4, 684
 Harris, C. R., Millman, K. J., van der Walt, S. J., et al. 2020, *Natur*, 585, 357
 Hey, D. R., Murphy, S. J., Foreman-Mackey, D., et al. 2020, *AJ*, 159, 202
 Hunter, J. D. 2007, *CSE*, 9, 90
 Hwang, H.-C., & Zakamska, N. L. 2020, *MNRAS*, 493, 2271
 Ijspeert, L. W., Tkachenko, A., Johnston, C., et al. 2021, *A&A*, 652, A120
 Jayasinghe, T., Kochanek, C. S., Strader, J., et al. 2021, *MNRAS*, 506, 4083
 Jayasinghe, T., Stanek, K. Z., Kochanek, C. S., et al. 2019, *MNRAS*, 489, 4705
 Jenkins, J. M. 2002, *ApJ*, 575, 493
 Jenkins, J. M., Chandrasekaran, H., McCauliff, S. D., et al. 2010, *Proc. SPIE*, 7740, 77400D
 Jenkins, J. M., Doyle, L. R., & Cullers, D. K. 1996, *Icar*, 119, 244
 Jenkins, J. M., Twicken, J. D., McCauliff, S., et al. 2016, *Proc. SPIE*, 9913, 99133E
 Johnston, C., Aymar, N., Abdul-Masih, M., et al. 2021, *MNRAS*, 503, 1124
 Johnston, C., Tkachenko, A., Aerts, C., et al. 2019, *MNRAS*, 482, 1231
 Kirk, B., Conroy, K., Prša, A., et al. 2016a, *AJ*, 151, 68
 Kirk, B., Conroy, K., Prša, A., et al. 2016b, *AJ*, 151, 68
 Kołaczek-Szymański, P. A., Pigulski, A., Wrona, M., Ratajczak, M., & Udalski, A. 2021, arXiv:2109.11508
 Kostov, V. B., Orosz, J. A., Feinstein, A. D., et al. 2020a, *AJ*, 159, 253
 Kostov, V. B., Powell, B. P., Orosz, J. A., et al. 2021a, *AJ*, 162, 234
 Kostov, V. B., Powell, B. P., Torres, G., et al. 2021b, *ApJ*, 917, 93
 Kostov, V. B., Welsh, W. F., Haghighipour, N., et al. 2020b, *AJ*, 160, 174
 Kovács, G., Zucker, S., & Mazeh, T. 2002, *A&A*, 391, 369
 Kruse, E., Agol, E., Luger, R., & Foreman-Mackey, D. 2019, *ApJS*, 244, 11
 Kurtz, D. W., Handler, G., Rappaport, S. A., et al. 2020, *MNRAS*, 494, 5118
 Lam, S. K., Pitrou, A., & Seibert, S. 2015, in Proc. Second Workshop on the LLVM Compiler Infrastructure in HPC, LLVM '15 (New York: Association for Computing Machinery)
 Laos, S., Stassun, K. G., & Mathieu, R. D. 2020, *ApJ*, 902, 107
 Li, J., Tenenbaum, P., Twicken, J. D., et al. 2019, *PASP*, 131, 024506
 Liakos, A., & Niarchos, P. 2017, *MNRAS*, 465, 1181
 Lintott, C., Schawinski, K., Bamford, S., et al. 2011, *MNRAS*, 410, 166
 Lintott, C. J., Schawinski, K., Slosar, A., et al. 2008, *MNRAS*, 389, 1179
 Mathieu, R. D., & Geller, A. M. 2009, *Natur*, 462, 1032
 Matijević, G., Prša, A., Orosz, J. A., et al. 2012, *AJ*, 143, 123
 Milone, E. E. 1968, *AJ*, 73, 708
 Moe, M., & Di Stefano, R. 2017, *ApJS*, 230, 15
 Morris, R. L., Twicken, J. D., Smith, J. C., et al. 2020, Kepler Data Processing Handbook: Photometric Analysis Kepler Science Document KSCI-19081-003
 Morton, T. D., & Johnson, J. A. 2011, *ApJ*, 738, 170
 Mowlavi, N., Lecoœur-Taïbi, I., Holl, B., et al. 2017, *A&A*, 606, A92
 Murphy, S. J., Bedding, T. R., Shibahashi, H., Kurtz, D. W., & Kjeldsen, H. 2014, *MNRAS*, 441, 2515
 Ochsenbein, F., Bauer, P., & Marcout, J. 2000, *A&AS*, 143, 23
 Orosz, J. A. 2015, in ASP Conf. Ser., 496, Living Together: Planets, Host Stars and Binaries, ed. S. M. Rucinski, G. Torres, & M. Zejda (San Francisco, CA: ASP), 55
 Orosz, J. A., Welsh, W. F., Haghighipour, N., et al. 2019, *AJ*, 157, 174
 Paardekooper, S.-J., Leinhardt, Z. M., Thébault, P., & Baruteau, C. 2012, *ApJL*, 754, L16
 Pedersen, M. G., Chowdhury, S., Johnston, C., et al. 2019, *ApJL*, 872, L9

- Pepper, J., Kuhn, R. B., Siverd, R., James, D., & Stassun, K. 2012, *PASP*, **124**, 230
- Pepper, J., Pogge, R. W., DePoy, D. L., et al. 2007, *PASP*, **119**, 923
- Pojmanski, G. 1997, *AcA*, **47**, 467
- Pollacco, D. L., Skillen, I., Collier Cameron, A., et al. 2006, *PASP*, **118**, 1407
- Pourbaix, D., Tokovinin, A. A., Batten, A. H., et al. 2004, *A&A*, **424**, 727
- Powell, B. P., Kostov, V. B., Rappaport, S. A., et al. 2021, *AJ*, **161**, 162
- Prša, A. 2018, *Modeling and Analysis of Eclipsing Binary Stars: The Theory and Design Principles of PHOEBE* (Bristol: IOP Publishing)
- Prša, A., Batalha, N., Slawson, R. W., et al. 2011, *AJ*, **141**, 83
- Prša, A., Guinan, E. F., Devlin, E. J., et al. 2008, *ApJ*, **687**, 542
- Raghavan, D., McAlister, H. A., Henry, T. J., et al. 2010, *ApJS*, **190**, 1
- Rappaport, S. A., Kurtz, D. W., Handler, G., et al. 2021, *MNRAS*, **503**, 254
- Ricker, G. R., Winn, J. N., Vanderspek, R., et al. 2015, *JATIS*, **1**, 014003
- Sahoo, S. K., Baran, A. S., Sanjayan, S., & Ostrowski, J. 2020, *MNRAS*, **499**, 5508
- Samus, N. N., Kazarovets, E. V., Durlevich, O. V., Kireeva, N. N., & Pastukhova, E. N. 2017, *ARep*, **61**, 80
- Sana, H., de Mink, S. E., de Koter, A., et al. 2012, *Sci*, **337**, 444
- Schmid, V. S., & Aerts, C. 2016, *A&A*, **592**, A116
- Schmitt, A., & Vanderburg, A. 2021, arXiv:2103.10285
- Sekaran, S., Tkachenko, A., Abdul-Masih, M., et al. 2020, *A&A*, **643**, A162
- Sekaran, S., Tkachenko, A., Johnston, C., & Aerts, C. 2021, *A&A*, **648**, A91
- Serenelli, A., Weiss, A., Aerts, C., et al. 2021, *A&ARv*, **29**, 4
- Shappee, B. J., Prieto, J. L., Grupe, D., et al. 2014, *ApJ*, **788**, 48
- Shibahashi, H., & Kurtz, D. W. 2012, *MNRAS*, **422**, 738
- Shporer, A., Fuller, J., Isaacson, H., et al. 2016, *ApJ*, **829**, 34
- Smith, J. C., Stumpe, M. C., Van Cleve, J. E., et al. 2012, *PASP*, **124**, 1000
- Southworth, J. 2015, in *ASP Conf. Ser.*, 496, *Living Together: Planets, Host Stars and Binaries*, ed. S. M. Rucinski, G. Torres, & M. Zejda (San Francisco, CA: ASP), 164
- Southworth, J., Bowman, D. M., Tkachenko, A., & Pavlovski, K. 2020, *MNRAS*, **497**, L19
- Stacy, A., Greif, T. H., & Bromm, V. 2010, *MNRAS*, **403**, 45
- Stassun, K. G., Oelkers, R. J., Pepper, J., et al. 2018, *AJ*, **156**, 102
- Stassun, K. G., & Torres, G. 2021, *ApJL*, **907**, L33
- Steindl, T., Zwintz, K., & Bowman, D. M. 2021, *A&A*, **645**, A119
- Streamer, M., Ireland, M. J., Murphy, S. J., & Bento, J. 2018, *MNRAS*, **480**, 1372
- Stumpe, M. C., Smith, J. C., Catanzarite, J. H., et al. 2014, *PASP*, **126**, 100
- Stumpe, M. C., Smith, J. C., Van Cleve, J. E., et al. 2012, *PASP*, **124**, 985
- Terrell, D., & Wilson, R. E. 2005, *Ap&SS*, **296**, 221
- Therrien, N., Hekker, S., Southworth, J., et al. 2018, *MNRAS*, **478**, 4669
- Thompson, S. E., Everett, M., Mullally, F., et al. 2012, *ApJ*, **753**, 86
- Tokovinin, A., Thomas, S., Sterzik, M., & Udry, S. 2006, *A&A*, **450**, 681
- Tonry, J. L., Denneau, L., Heinze, A. N., et al. 2018, *PASP*, **130**, 064505
- Torres, G., Andersen, J., & Giménez, A. 2010, *A&ARv*, **18**, 67
- Twicken, J. D., Clarke, B. D., Bryson, S. T., et al. 2010, *Proc. SPIE*, **7740**, 774023
- Virtanen, P., Gommers, R., Oliphant, T. E., et al. 2020, *NatMe*, **17**, 261
- Wells, M. A., & Prša, A. 2021, *ApJS*, **253**, 32
- Welsh, W. F., Orosz, J. A., Aerts, C., et al. 2011, *ApJS*, **197**, 4
- Welsh, W. F., Orosz, J. A., Carter, J. A., et al. 2012, *Natur*, **481**, 475
- Wheeler, A., & Kipping, D. 2019, *MNRAS*, **485**, 5498
- White, T. R., Benomar, O., Silva Aguirre, V., et al. 2017, *A&A*, **601**, A82
- Wilson, R. E. 1994, *PASP*, **106**, 921